Chapter 3
Neutron Optics and Detectors

P. S. Sarkar and Yogesh S. Kashyap

Introduction

Despite recent progress in the development of advanced and improved neutron sources, neutron-based experiments continue to be severely constrained by available neutron fluxes at various neutron facilities. Currently, the majority of neutron sources are either reactor-based (with power ranging from 1 to 100 MW) or accelerator-based, employing the spallation process (beam power 1 MW). Typically, the peak neutron flux at the core is in the range of 10^{13} to 10^{15} n/cm^2/s, with this range being limited mostly by target cooling or heat removal concerns. As a result, the neutron flux at the sample location typically varies between 10^6 to 10^9 n/cm^2/s. In comparison, X-ray flux at the sample locations in the contemporary synchrotron radiation-based X-ray sources varies between 10^8 to 10^{13} photons/s/mm^2/mrad^2/0.1% bandwidth. This means that neutron sources have a brightness several orders of magnitude lower than X-ray sources, and their phase space density is 1000–10,000 times smaller than X-ray phase space density. Therefore, in absence of extremely high brightness neutron sources, the advancement in neutron optics and the related instruments is of vital importance for efficient use of current generation of neutron sources [1].

Broadly speaking, one can classify neutron optics into the following major classes, based on their interaction with the material medium as shown in Fig. 3.1.

The Neutron optics is based on assigning a complex refractive index to the materials as $n = 1 - \delta - i\beta$. Neutron interactions with most materials are quite weak, resulting in a refractive index that is extremely close to unity. As a result, neutrons only reflect from surfaces at grazing angles, which are usually only a few degrees. Consequently, fabrication of efficient neutron optical components like lenses and

P. S. Sarkar (✉) · Y. S. Kashyap
Technical Physics Division, Bhabha Atomic Research Centre, Mumbai 400085, India
e-mail: pss@barc.gov.in

Y. S. Kashyap
e-mail: yskashyap@barc.gov.in

D. K. Aswal et al. (eds.), *Neutron Imaging*,
https://doi.org/10.1007/978-981-16-6273-7_3

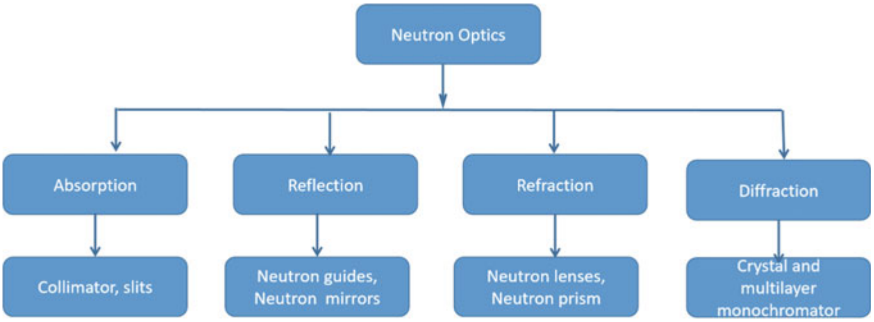

Fig. 3.1 Showing different types of neutron optics and the basic interaction mechanism

mirrors, which are often employed in visible-light optics, is quite challenging. We will briefly discuss a few of the optical elements relevant for neutron imaging.

3.1 Absorption-Based Optics

3.1.1 Neutron Collimators

Usually, the moderated neutrons from the reactor core are transported through the reactor shielding via hollow beam tubes or neutron guides. These extracted neutrons have the Maxwellian velocity distribution with average energy dependent on moderator temperature and an angular spread defined by the external collimation imposed on the beam. As the volume of the thermalized neutron in the moderator is enormous compared to the sample dimensions, one needs to have an efficient means to deliver the neutron beam of well-defined size and divergence for carrying out any measurement. A collimator is a passive device that filters a beam of neutrons so that only those travelling in a defined solid angle or directions are transmitted to the sample position. Usually, the type of collimators can be classified into three types namely, parallel collimator, diverging collimator and converging type collimator. An illustration with a cut-away view of a typical divergent collimator is shown in Fig. 3.2. Neutron radiography collimators typically included the following components:

(a) **Illuminator**—The role of the illuminator is to create a homogeneous neutron source. Normally, it is a 10–15 cm thick graphite or polythene block positioned at the beginning of beam tube to boost the thermal neutron flux entering the collimator.

(b) **Beam filters**—These filters are mostly used to remove or filter gamma rays and fast neutrons from the beam. Because of its low neutron attenuation and strong gamma-ray attenuation characteristics, Bismuth (Bi) is widely employed for gamma-ray filtering. Furthermore, to improve thermal neutron transmission, Bi is frequently utilized in a single-crystal structure. Similarly, single-crystal

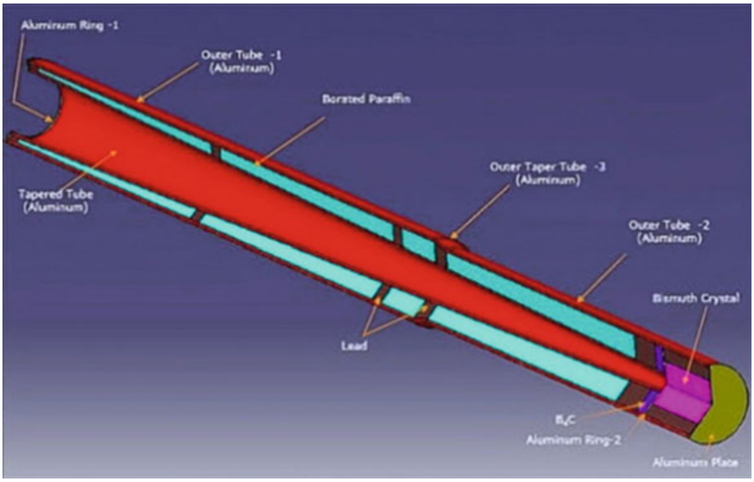

Fig. 3.2 Example of a divergent neutron collimator

Sapphire (Al_2O_3) and/or Silica (SiO_2) are often used to reduce the high energy neutron content travelling to the experimental hutch.

(c) **Aperture**—The aperture defines the pinhole in the pinhole camera analogy, which is frequently used to characterize collimator design. The pinhole size determines the maximum flux at the sample position and point spread function of the neutron imaging instruments. As the thermal neutrons should not be allowed to enter the beam tube other than through the pinhole, it's constructed of materials such as Gd, Cd, which have very high thermal neutron absorption cross-section.

(d) **Gamma shielding/cleanup plates**—Pb-based gamma shielding is commonly used, however heavy concrete or other materials may also be used. Moreover, to prevent streaming, gamma shielding is installed at every step change in beam-tube dimension. Similarly, in order to prevent capture gammas and scattered neutrons from reaching the experimental hutch, boron-based material in the form of plates is often employed in conjunction with lead sheet.

(e) **Filling gas**—It's worth noting that neutron scattering from nitrogen in the air decreases the neutron intensity at the sample by 5% per metre. These scattered neutrons not only degrade the sharpness of the neutron image or increase the background, but also interact with the collimator walls resulting in emissions of secondary gamma rays, that require further shielding. As a result, collimators are frequently either evacuated or filled with Helium.

3.1.2 Velocity Selector

A velocity selector is a mechanical device that allows only neutrons of certain wavelength or velocity to get transmitted through. The velocity selectors can be of the solid drum type with helical slot or of the multidisk type. A disk-type velocity selector device works on the principle of chopping of the incoming neutron beam twice in succession, at two different points separated by suitable flight path. Usually, the disks are displaced by certain angle (θ), therefore the neutrons transmitted by the first disk will be stopped by the second one if at rest. The second disk will transmit those neutrons whose velocity is equal to the distance between the two disks divided by the time corresponding to the rotation of disk by the angle (θ). Usually, more than two disks are used in modern devices and the selection of neutron energy is achieved by varying the speed of rotation. The number of disks and number of slots and its width is decided depending upon energy range and energy resolution requirement of the experiments. Another type of velocity selector uses absorbing radial blades, like multiple peripheral slits, usually set at certain angle to the incoming beam. When the device is stationary the neutrons will get completely absorbed and will get transmitted only if the device is rotating. Photograph of a typical mechanical velocity selector is shown in Fig. 3.3. Velocity selector performs a coarse monochromatization, and typical values are about 10–30% of the mean wavelength. The transmission of neutron through a velocity selector is determined by its geometrical parameters. The transmitted wavelength ($\lambda = K/\omega$) is inversely proportional to the rotational speed (ω), where K is a constant. The selector's geometry and the tilt angle between the selector axis and the neutron beam determine the constant (K). Another useful device based on the absorption optics is the Fermi chopper first proposed by Fermi in the 1940s, which is nothing but a rotating shutter consisting of neutron-absorbing and neutron transmitting materials placed into a very fast revolving cylinder. It can be used to obtain pulsed monochromatic beam of neutrons at the accelerator-based neutron sources or in combination of monochromator crystals at the reactor-based neutron sources.

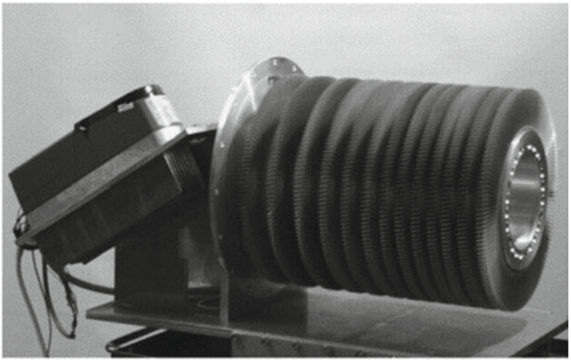

Fig. 3.3 Example of mechanical velocity selector (reproduced from [2] © 2004, with permission from Elsevier)

3.1.3 ^{3}He Spin Filter for Neutrons

Polarized neutrons are widely used in neutron scattering and polarized neutron imaging experiments. Usually, neutrons with a specific spin orientation are chosen using suitable neutron optics, and their orientation after passing through the magnetic field region or sample is recorded on the neutron detector, which is positioned immediately after the neutron analyzer. The spin of scattered, transmitted, or reflected neutron after passing through the sample is analyzed to generate the neutron depolarization data, which in turn provides information about magnetic properties of the sample. The basic idea to obtain the polarized neutron is through spin dependence of magnetic scattering [3], nuclear scattering [4] or resonant neutron capture [5]. Absoprtion based polarized neutron spin filters are based on the spin-dependent absorption of neutrons by ^{3}He, and can produce a polarized neutron beam over a wide range of neutron wavelengths. The resonant absorption of the neutrons depends on compound nuclear spin states, $I + 1/2$ and $I - 1/2$, where I is nuclear spin before the neutron capture. The spin orientations of the nuclear and neutron spins affect the absorption of neutrons by ^{3}He; if the nuclear and neutron spins are anti-parallel, the absorption is extremely high. If the spins are parallel, however, there is far less absorption. The transmission of spin-parallel neutrons and spin anti-parallel neutron beam through polarized ^{3}He cylindrical cell can be simply expressed as $T_{\pm} = \exp\{-(1 \mp P)n\sigma l)$ where P is the ^{3}He nuclear polarization, n the number density of ^{3}He atoms, σ the absorption cross-section for unpolarized neutrons (σ_0 [barn] ≈ 3000 · λ [Å]) and l is the length of the spin filter cell. Polarized ^{3}He is typically produced through metastability-exchange optical pumping (MEOP) [6] or spin-exchange optical pumping (SEOP) [7]. Figure 3.4 shows the Photograph of a typical ^{3}He cell was fabricated at J-PARC.

Fig. 3.4 ^{3}He cell fabricated at J-PARC (reproduced from [8] © 2020, with permission from Elsevier)

3.2 Reflective Optics

3.2.1 *Neutron Mirrors*

The neutron mirrors usually operate on the principle of total external reflection in exact analogy with the conventional light optics. However, in case of neutrons these mirrors work mostly in the grazing incidence mode due to small refractive index ($n \sim 10^{-6}$) of most of the materials for neutrons and they reflect the neutrons with wavelength greater than critical wavelength. As the refractive index depends upon the wavelength of the neutrons (λ^2), the mirrors are therefore most suitable for longer wavelength neutrons such as thermal or cold neutrons. Usually, neutron mirrors are used as focusing devices to effectively utilize the incoming neutron by efficiently converging them onto samples or detectors, thus improving flux density. The neutron focusing optics includes parabolic mirrors, elliptic mirrors, Kirkpatrick–Baez mirrors, Wolter mirrors, etc. [9]. Generally, neutron-focusing mirrors use supermirror coating, to reflect slow neutrons over a wide spectral range. Another completely different approach as suggested by Kumakhov [10] is to use thousands of glass capillaries and guide these neutrons using multiple reflections and thereby focusing the beam to a spot with a diameter less than 1 mm. Another recent development is the demonstration of novel neutron focusing optics based using Wolter optics suitable for use in neutron imaging and small-angle scattering experiments. The axisymmetric grazing-incidence focusing mirrors using identical pairs of confocal coaxial Hyperboloid and Paraboloid can improve the resolution of conventional neutron imaging camera to achieve sub-micron level resolutions [11]. Its schematics is shown in Fig. 3.5.

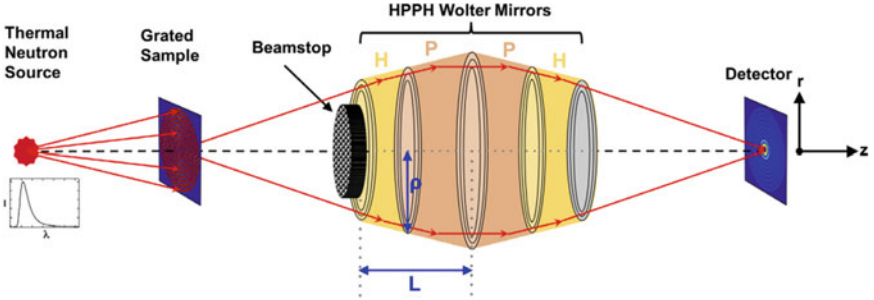

Fig. 3.5 Schematics of the neutron microscope optimized for thermal neutrons (reproduced from [11] © 2017 with permission from Elsevier)

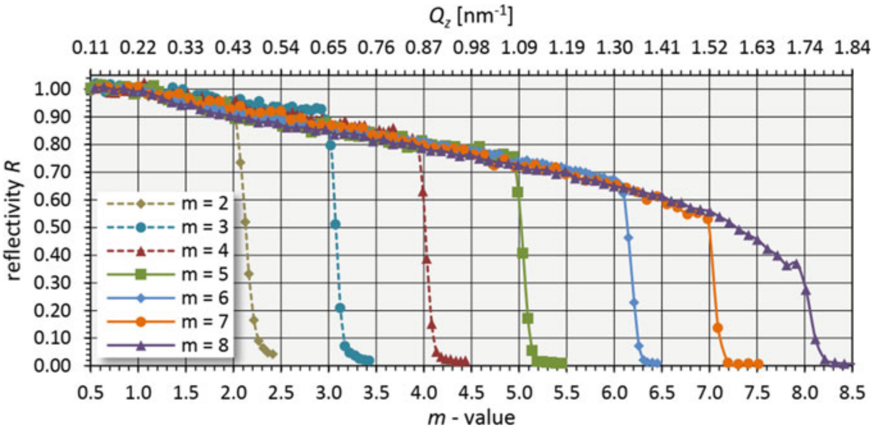

Fig. 3.6 Neutron reflectivity of a supermirror on a refined aluminium substrate (diamonds) and float glass (squares), with Ni/Ti supermirror [13]

3.2.2 Neutron Supermirror

These multilayer mirrors are constructed from alternating layers of two materials with different neutron scattering lengths. Alternating layers of materials such as nickel and titanium are deposited on a glass substrate to create these mirrors. Supermirrors, thus are a kind of multi-layer neutron mirror, with variable layer thicknesses. The advantage of this variable lattice spacing is that a neutron beam travelling through these layers encounters variable one-dimensional optical potentials. As a result, as the neutron beam transverses through these layers partial reflection and transmission of a neutron wave occur at every interface, resulting in the appearance of multiple waves within the system. By slowly varying the period of multilayer structures, the effective reflection angle can be larger than the total reflection angle. This idea was realized by Mezzi for extracting thermal neutrons with a sufficiently wide wavelength range. Ni/Ti is the materials system of choice for broadband neutron multilayer supermirrors due to the small absorption coefficient and large difference in the real part of the refractive index, with low values for the imaginary part.

One of the most important properties of a supermirror is its critical angle, θ_c^M the angle up to which it reflects and it is determined by the thickness of the thinnest layer. By convention it is measured in multiples (m) of the critical angle of natural nickel. The reflectivity of a mutilayer is generally proportional to the fourth power of its thickness and the square of the number of layers. As a result, the number of layers required to achieve the same reflectivity for a given bilayer thickness grows quadratically as the thickness decreases. The first neutron supermirror concept was proposed by Mezzi [12] inspired by earlier work with X-rays.

Hosobata et al. [14] have reported the development of precision elliptic neutron-focusing supermirrors. The evaluation experiments carried were carried out on BL16

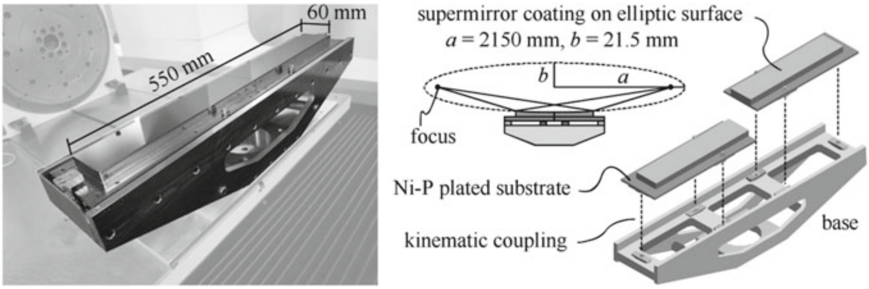

Fig. 3.7 An example of elliptic neutron-focussing mirror [14]

at the Materials and Life Science Facility, J-PARC, Japan and showed 68–90% reflectivity at a critical angle. The photograph of the developed supermirror is shown in Fig. 3.7.

The Polarizing multilayer supermirrors were reported by Lynn et al. [15]. The refractive index of neutron for magnetic materials can be expressed as

$$n^2 = 1 - \lambda^2\left(\frac{Nb_c}{\pi} \pm \frac{2m\mu_n B}{h^2}\right)$$

where N is particle density, b_c is average bound coherent scattering length, m and μ_n are mass and magnetic moment of neutron, h is Plancks constant and B is saturation induction of the magnetic material. For ferromagnetic materials, one can simplify the above expression as

$$n^2 = 1 - \frac{\lambda^2 N}{\pi}(b_c \pm b_m)$$

where b_m can be considered as effective magnetic scattering length. This shows that neutron with two different spins directions will interact very differently and for $b_c = b_m$, the reflected beam is completely polarized. Polarizing supermirrors make use of the fact that the scattering lengths of the two spin components in ferromagnetic materials are extremely different. Thus the idea of index matching, in addition to the property of two distinct scattering lengths, is employed in polarizing mirrors. A thin film of ferromagnetic material is deposited on a substrate whose refractive index matches that of the film, for only one of the two spin components of incoming beam of neutron. Under this condition, there will be no optical density difference between the ferromagnetic layer and substrate layer, and hence one of the spin component will get transmitted to the substrate layer. Therefore one of the spin component is then removed from the beam by absorption or by incoherent scattering, while the other spin component undergoes total external reflection at the magnetic layer, and hence polarized neutron beam can be obtained. The layer sequence is calculated based on the contrast of two materials for the one spin component, after selecting

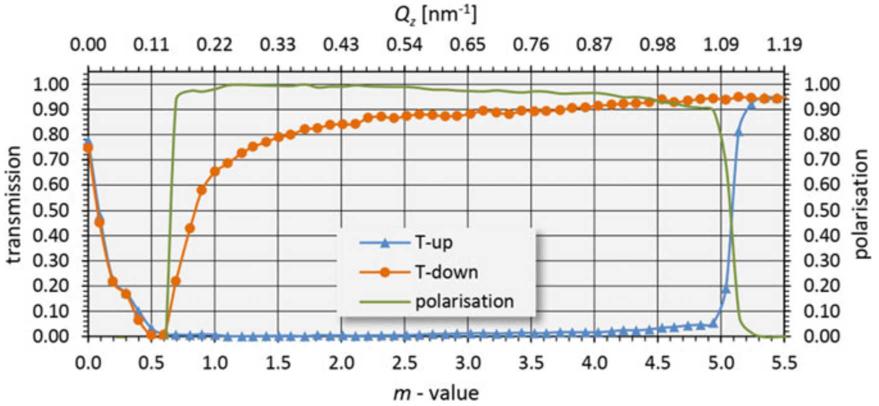

Fig. 3.8 Spin-dependent transmission and polarization of a polarizing supermirror Fe/Si with $m = 5$ coated on both sides of a Si wafer with a thickness $t = 0.3$ mm [13]

two materials with the same scattering length density. In most cases, polarizations of up to 98% are possible, while the polarized beam intensity of 30–40% of incident neutron beam intensity (Fig. 3.8). Historically, the material pairs Fe–Ag and Co–Ti were used to create the first polarizing mirrors. Fe–SiN_x and $Fe_{89}Co_{11}$–Si or Co–Ti, FeCo–TiZr, and $Fe_{50}Co_{48}V_2$–TiNx [16–18] are two of the most frequent supermirror combinations utilized nowadays.

3.2.3 Neutron Guide

The neutron guides work in the same way that of optical fibres: neutrons are transported through the neutron guide tube by total external reflection; only those neutrons which enter the guide with an angle of incidence that is smaller than the critical angle (depending upon their wavelength) will pass through the guide by repeated total reflections. For a non-magnetic material, the relation between critical angle (θ_c) and coherent scattering length (b_c) is given by:

$$\theta_c = \lambda\sqrt{\frac{Nb_c}{\pi}}$$

where λ is neutron wavelength and N is the N is the number of atoms per unit volume. The value of critical angle for representative material like for Ni is ~ 0.1° λ(Å). The guide tube usually has a little curvature to ensure that only slow neutrons with a wavelength higher than a certain value are guided towards exit of the guide tube. Fast neutrons or neutron with shorter wavelengths, as well as any gammas in the incident beam, pass through the guide tube wall and are usually absorbed in the shielding that surrounds it. This permits a very clean and highly collimated beam of slow neutrons

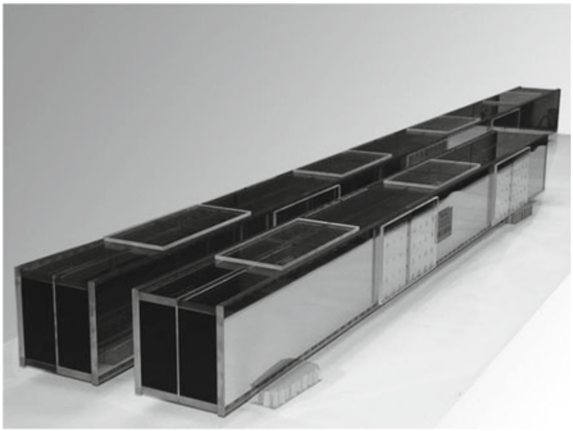

Fig. 3.9 Photograph of the neutron guide (reproduced with permission from Mirrortron Ltd.)

to be delivered from the original neutron source to the far away experimental station. As a result, using a neutron guide allows for extremely low background radiation, which is ideal for high precision neutron scattering and imaging experiments. Another advantage of the guide is that it can deliver neutrons to several instruments at the same time in a low-background environment. Moreover, the flux at the end of a neutron guide being proportional θ_c^2, therefore one can significantly improve the flux by using supermirror coatings such as Ni–Ti. Supermirrors consisting of 2600 Ni–Ti leading to refection angles more than $4\theta_c^{Ni}$ and reflectivity greater than 80% have already been achieved [13, 19]. Similarly, neutron guide made out of ferromagnetic material magnetized to saturation, it is possible neutron arriving at the exit of the guide tube is polarized. Such polarized neutron guides have been demonstrated with Fe–Co and Ti–Gd deposited on basic guide material. Photograph of a typical neutron guide is shown in Fig. 3.9.

3.3 Refractive Optics

3.3.1 Neutron Lenses and Prisms

A well-known phenomena in geometric optics is the refraction of a light at an interface with two different refractive indices. Neutron beams refract in the same way at the interfaces of different materials; but, as previously stated, neutrons have a very low refractive index for most materials, thus this effect requires a large number of interfaces for any practical uses. Therefore we need an array of refractive elements to focus the neutrons in a meaningful way. The first refractive lens was made using an array of 30 biconcave lenses from MgF_2 [20]. The advantage of the refractive lenses is that they can be placed directly in the beam path and are easy to align. Figure 3.10 shows a photograph of a 6- and 28-element array of symmetric spherical

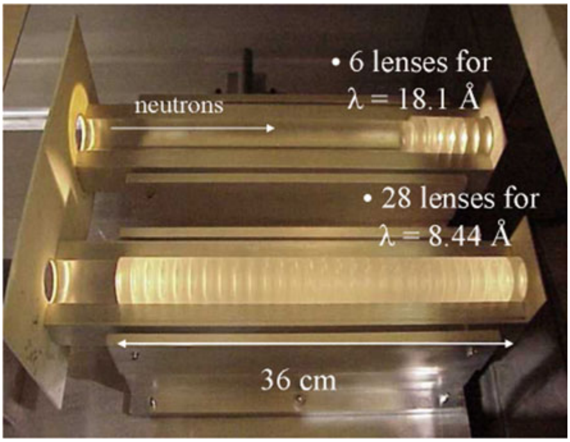

Fig. 3.10 Photograph of the 6/28 element array of 25-mm-diameter symmetric spherical MgF_2 biconcave lenses [24]

MgF2 biconcave lenses with a diameter of 25 mm. It may be noted that neutron transmission through these lenses decrease diagrammatically for larger beam size or larger neutron beam path, due to the lens shape effect. As a result, to address this issue, Fresnel lenses made of vitrous silica and MgF_2 single crystals have also been developed [21]. Similarly, compound refractive prism for cold neutrons made of MgF_2 single crystal have also been fabricated and with 50 single-sided lens element assembly, transmission of 0.83 with a focal length of 5 m for 1.14 nm neutrons was reported [21]. The focusing and polarization of neutrons by magnetic induction has been explored in the development of a magnetic compound refractive lens composed of 99 pairs of cylindrical permanent magnets in order to increase the focused intensity of a polarized white beam of cold neutrons. [22]. Recently, imaging of objects with very cold neutrons, using novel, permanent magnet ($Nd_2Fe_{14}B$) compound refractive lenses (MCRL) with a large 25 mm bore diameter has also been reported [23].

In order to overcome the absorption of the neutron in the convention refractive optics and diffuse scattering in the reflective optics, magnetic compound refractive lenses and prisms using have also been developed. The magnetic compound refractive lens consists of voids and magnetic field regions and it provides focused spin polarized neutrons. However, a magnetic refractive lens can focus only neutrons with spin parallel to the magnetic field, while neutrons with anti-parallel spins diverge, and therefore only 50% of neutron flux is available for the experiment, if the input beam is unpolarized. Shimizu et al. [25] used permanent magnets to demonstrate the feasibility of such a lens towards attaining intensity gain of 35 at 14.4 Å neutron wavelength, and further superconducting sextupole magnet (SSM) with Nb/Ti superconducting coils have been successfully demonstrated with cold neutrons. Development of lenses based on a permanent sextupole magnet with continuous field modulation via a rotating double-ring structure, called modulating permanent-magnet sextupole (mod-PMSx) [26–29] have also been reported. The feasibility of mod-PMSx for high resolution imaging through magnification has also been proven [29].

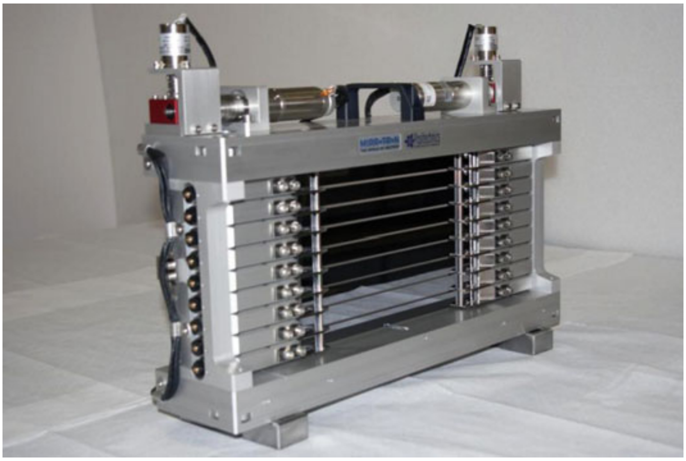

Fig. 3.11 Multiple single crystal based neutron monochromator (reproduced with permission from Mirrortron Ltd.)

3.4 Diffractive Optics

3.4.1 Crystal Monochromator

The monochromator is one of the most important optical components in almost all the reactor-based neutron instruments. A neutron monochromator is a device made up of a single or double crystal that receives polychromatic neutron beams and provides a specific wavelength at sample locations based on Bragg's rule. The wavelength range accepted by a monochromator is determined by its crystal structure and mosaicity. A higher mosaicity increases the integrated flux of neutrons that reach the sample, however, it reduces the wavelength resolution of the instruments. As shown in Table 3.1, most commonly used materials as monochromator crystals include pyrolytic graphite (PG), silicon (Si), copper (Cu), beryllium (Be), and Heusler crystals. The monochromator crystal is usually selected depending upon the incident energy range

Table 3.1 Examples of some materials used as single crystal monochromator

S. no.	Crystal	d-spacing (A)
1	PG (002)	3.35
2	Be (002)	1.79
3	Cu (220)	1.28
4	Ge (111)	3.27
5	Si(220)	1.92
6	Si(111)	3.13
7	Heusler (111)	3.44

required for the experiment and the desired energy resolution. The double-crystal monochromator with highly oriented pyrolytic graphite HOPG (002) single crystals has been demonstrated to be a useful device for energy-resolved imaging and Bragg-edge imaging applications. The benefit of this configuration is that the outgoing monochromatic neutron beam remains parallel to initial incoming neutron beam even when the wavelength of neutron is varied, simplifying the experimental setup.

On the other hand, neutron diffraction experiments require focussed neutron beams at the sample positions, and hence bent single crystal is used. Due to the size of neutron beams, very large single crystals are required for neutron monochromators, e.g. 10^5 mm^3. However, as the neutron beams are of relatively low intensity, and single crystals have too small band-pass ($\Delta\lambda/\lambda$), to accept large neutron beam, multiple single crystals are used, as illustrated in Fig. 3.11. This not only helps to increase the crystal size but allows a large degree of bending without approaching the breaking limits of the material. A more recent development is to produce very fine slices of single crystal, and to glue them together in near-perfect alignment, thus simulating on a rather large scale the effect of mosaic blocks.

3.4.2 Neutron Filters

Whan a neutron beam is passed through a system consisting of polycrystalline material, for $\lambda \leq 2d$ (d: interplanar spacing, λ: wavelength), the condition of Bragg scattering is always satisfied, leading to the removal of neutrons below this wavelength. On the other hand $\lambda \geq 2d$, and there would be no Bragg scattering and the beam will be transmitted. For a sufficiently large crystal, the effect will be the same as that sample is absorbing the neutrons with $\lambda \leq 2d$, while all the other wavelengths are transmitted and the crystal will act as a neutron wavelength filter. One can therefore arrange two such crystal materials with similar $2d$ spacing such that only a window of the wavelength is transmitted. Some useful polycrystalline materials are Be and BeO, which are usually used to select neutrons above 4 Å. On the other hand, some single crystals such as Bismuth, Sapphire, etc. are used as filters for spectral shaping in neutron imaging beamlines. Bismuth single crystal is usually employed in the reactor to block the incoming gamma rays and improve the neutron to gamma ratio. Sapphire (α-Al_2O_3) crystal exhibits some unique properties such as High Debye-Temperature (1047 K), high transmission of thermal neutrons, which help in improving the thermal neutron content at the experimental station by scattering out epithermal and fast neutrons. Figure 3.12a shows simulated total neutron cross-section per molecule of α-Al_2O_3 and Fig. 3.12b per atom of bismuth at 300 K, without the coherent elastic (Bragg) scattering part.

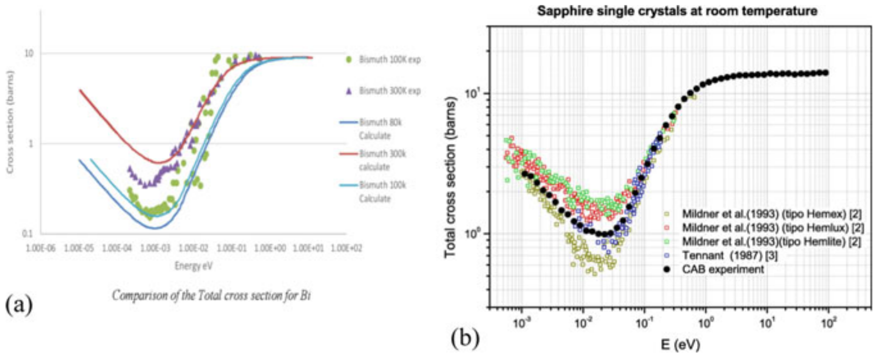

Fig. 3.12 Total neutron cross-section at 300 K for **a** Bismuth single crystal [30] (Al_2O_3) and **b** Sapphire single Crystal filter [31] (reproduced from [31] with permission from Copyright © 2015 Elsevier Ltd.)

3.5 Neutron Detection: Basic Principle and Methodology

Since neutrons have no charge, their interaction is through nuclear interaction and as they are not perturbed by the atomic electrons they can penetrate deeper into the materials. But this charge neutral status of neutrons makes their detection difficult. For detection of neutrons, they must interact and be absorbed by certain elements having high interaction (scattering/nuclear reaction) cross-section and the resulting particle(s) emitted from these reactions, deposit their energy and produce detectable emission(s). This forms the basis of neutron detection. As the cross section for neutron interactions in most materials strongly depends upon neutron energy, different techniques have been developed for neutron detection in different energy regions. The neutron energies can be roughly divided into two groups—slow neutrons which have energy below the cadmium cut off (0.5 eV) and fast neutrons with energy above this level. Based upon the methodology and application for neutron detection, the detectors can be subdivided into two groups: passive and active.

The interaction probability for thermal neutrons is high for elastic scattering such as $X(n, n)X$ and their detection is not possible owing low energy transfer via this mechanism. In case, the neutron energy is sufficient to impart some of its energy to the interacting nucleus, the recoil nucleus ionizes the surrounding medium which then produces some signal to be detected. Neutron-induced nuclear reactions are the mechanism by which charge particles are generated towards production of detectable signals in terms of scintillation or fluorescence. Possible outcome of neutron interaction with a target nucleus may be any or combination of various processes such as recoil nucleus, protons, charge particles, conversion electrons, gamma, fission fragment.

For thermal neutrons the materials having high absorption cross-section are ^3He (5333 b), ^6Li (940 b), ^{10}B (3835 b), Cd (^{113}Cd (12% abundance): 20743 b) and Gd

(^{157}Gd (15.7% abundance): 255011 b, ^{157}Gd: 60,791 b). He-3 and B-10 based gas-based detectors are in general used for monitoring and detection purposes though recent developments cite gas-based imaging detectors.

We here restrict ourselves to neutron detectors for imaging purposes only. For completeness, basic neutron detectors used for dose monitoring towards operational as well as personnel safety are mentioned in brief.

Neutron converters are the first most important part of neutron detection. They must have the following properties to qualify as suitable neutron converters. These are high interaction cross-section, creation of detectable signal in accordance with the used phosphor, reaction Q value must be high for good discrimination in mixed radiation fields and most importantly the material should be transparent to the emitted detectable photons. The materials which generate high mass charge particles on interacting with the neutrons are the most suited for imaging detectors because of two reasons; firstly their energy deposition will be more hence more light which in turn provide higher signal content and secondly owing to their less travel path localization of light signal takes place which translates to achieving higher spatial resolution.

Examples of various class of neutron imaging detectors are films, image plate, gas-based detectors, scintillator screens, single crystals and semiconductor detectors. Initial work on the development of area-based neutron detectors started with activation foils (Gadolinium, Dysprosium and Indium) and then transfer the image to a phosphor coupled with a photographic film. Development of neutron sensitive image plates (BaFBr(Eu):Gd_2O_3) on the lines of X-ray image plates were developed. Later on, neutron image scintillator screen having ^{6}LiF:ZnS(Ag)/Gd_2O_3 in Lucite were developed and made commercially available. Till date ^{6}LiF:ZnS(Ag) screens are the most widely used in combination with high resolution as well as cooled Charge Coupled Device (CCD) or CMOS cameras or semiconductor panels in various configurations to yield digital neutron images. In case the neutron flux falling onto the detector is low, image intensifiers are used to amplify the signal content but with an amplification in the noise content too. There has been constant development with newer materials or their combinations towards aiming high resolution, high image contrast and improved radiation hardness. Though thermal neutron radiography had been the mainstay technique for a long time, with the availability of high flux neutron sources like the spallation sources or high flux research reactors, the quest to look more deeper inside bulk materials with high resolution through high collimation factor without compromising on neutron numbers, carrying out dynamic imaging with high temporal resolution, high detection efficiency thereby decreasing experimentation time as well as increasing contrast has motivated the concerned scientific community towards development of better-improved neutron imaging detectors. Thrust was put on material research with an aim to develop new materials or their combination and even combining multiple detector technologies towards hybrid detector development providing information which were thought to be impossible to obtain a decade back. Moreover, with the advancement in computer technology, faster and robust data acquisition, archiving and analysis have prompted use of complex analysis methodologies in implementing imaging with such hybrid detectors. For example, the advanced highly efficient charge particle detectors developed for various particle accelerator programs were suitably modified by coupling with some neutron converter material such as ^{6}Li, ^{10}B or ^{157}Gd. They proved to be excellent high-resolution pixelated imaging detectors. Their throughput was also very high owing to their reduced read-out time. Medipix-2, nGEM and LiTA12 are some examples of such detectors. Special FPGA electronics and data acquisition including analysis techniques were also part of these developments. ^{3}He and BF$_3$ based gas detectors are already proven neutron detectors used for counting applications and dose measurements. A clever move by configuring these with multiwire proportional counter methodology and 2D read-out, produced gas-based hybrid detectors towards neutron imaging applications. Since these detectors are current based, appropriate mechanisms to incorporate high gain could be easily realized. μPIC, μNID are some newer detectors developed on this principle.

Application-specific imaging detector development is governed by various parameters. They are pixel size, dynamic range, frame rate, readout speed, overall noise (dark, white and readout), data readout mechanism, compatibility with existing protocols and finally the cost. All these factors are interlinked in some way or the other and an optimum solution is sought with all possibly achievable ones. Let's elaborate it a bit more. Since neutrons are of low interacting type, in the case of scintillator screens if the neutron converter thickness is increased (say 200–300 μm) to increase detection efficiency, light spread increases resulting loss in spatial resolution. On the contrary for very thin (say < 50 μm) scintillator screen, the achieved spatial resolution is high (~ screen thickness), but the light output is low which increases image acquisition time and this in turn increases photon detector noise. Detector throughput may not be that important for simple radiography but for tomography applications when a large number of projections are to be acquired, it is of great interest.

Various parameters linked to imaging detectors [32, 33] deciding their performance capability are linearity, response time, quantum efficiency, pixel size, gain, noise characteristics and dynamic range. The imaging system as a whole is qualified by parameters such as spatial resolution, Modulation Transfer Function (MTF), Detective Quantum Efficiency (DQE), Signal to Noise Ratio (SNR) and Noise Power Spectrum (NPS). The terms are discussed below.

Linearity: In radiation imaging detectors the signal output must be linear with the dose, equivalent to the number of radiation quanta, falling on it. For any detector, there is a linearity range defined by the manufacturer. The linearity is also dependent on the energy of the radiation quanta falling on it.

Response time: This is the time taken by the detector to generate response signal, after the interaction with the radiation, to be converted to measureable data. In the case of neutron imaging, the dependencies for response time are converter material property towards signal generation, methodology of coupling with photo-detector and its response characteristics.

(A) **Pixel size**: This is the smallest unit of the detector which generates signal proportionate to active volume/size and in combination with such large numbers of its replica forms the entire detector.

(B) **Quantum efficiency**: This term signifies the probability of primary ionization taking place as soon as it interacts with detector material.

(C) **Gain**: This parameter signifies the amplification introduced in the detector's signal generation module. This is helpful in case where sufficient signal does not exist to provide good quality images.

(D) **Noise**: The unwanted data associated with the actual signal decreasing its worthiness is called noise. The signal is represented by the number of incident particles and the noise associated with it the square root of the signal. The contributors towards noise are: (a) shot noise arising from the statistics of the signal generating process, (b) readout noise associated with the signal readout mechanism and (c) dark noise contributed by the background effects such as background radiation either same (scattered) or of other types. Shot noise decreases as the input radiation intensity increases, faster readout increases the noise and background or dark noise can be decreased by other cooling the detector and/or shielding to reduce such effects. The methodology to be implemented is different for different detectors.

(E) **Dynamic range**: This parameter designates the maximum number of discrete values the signal can be sampled to provide meaningful representations of variations present in the signal. In digital detectors, this is governed by the A/D converter and associated electronics. As, for example, an 8bit image contains 256 shades and a 16bit image contains 65,536 shades, each shade to shade variation brings in some contrast. So more the bit depth, more is the information and hence more discernible contrast embedded in the image.

(F) **Signal to Noise ratio (SNR)**: Denoted as S/N, this parameter signifies the signal level with respect to the noise. S/N must be high to obtain good quality data as well as good quality image. Though increasing exposure increases the signal strength but at the cost of increase in noise.

(G) **NPS**: This parameter determines the spectral density of the noise as a function of spatial frequency. Here spatial frequency is the inverse of the lengths, defined by the feature sizes looked into or imaged, in the spatial domain. Fine features in the spatial domain signifies high frequency component in the spatial frequency domain.

(H) **MTF**: This parameter describes how faithfully the detector as a unit translates the input signal to the image domain towards providing information being sought. MTF is described in terms of percentage contrast at a certain line pair per unit distance.

(I) **DQE**: In the case of imaging detectors, DQE [34, 35] is defined by the ratio of squared out SNR to the squared input SNR. With N number of radiation quanta falling on the detector and if N' numbers of such quanta are utilized to generate image information then the DQE of the detector is said to be N'/N. This measures the efficiency of the detector in terms of the degradation of the input SNR after being converted into image by the detector or the imaging system. For a detector with DQE = 1, all the input radiation has been translated into image information. DQE is dependent on detector construction, radiation exposure, spatial frequency and MTF.

Though the parameters such as DQE, NPS and MTF are evaluated in general for X-ray detectors as per the international standard IEC 62,220–1[36], the same is not strictly followed by all for neutron imaging detectors. It is worth mentioning that NR community has accepted MTF as the figure of merit as far as spatial resolution determination is concerned. But MTF alone is insufficient to determine image quality as it does not consider the noise components. In this regard, DQE which is deduced by taking into account both the noise and contrast information is the metric that can provide the ability of the detector towards fine feature detection. Masalovish [37] has suggested formula for evaluating DQE of a neutron image plate and optimize the exposure time for obtaining desired image quality. Radoslaw Lewandowski, Lei Cao, Danyal Turkoglu [38] have provided methodologies towards evaluation of DQE at NIST 20 MW research reactor using ^{6}Li-ZnS scintillator screen coupled with a digital camera as imaging unit and beam purity indicator as the standard test sample.

3.6 Neutron Detectors for Imaging Applications

3.6.1 Film Based Detectors

Nitrocellulose and X-ray-based films have been in use for ages for gamma/X-ray imaging in basic and applied science applications. Neutrons have very little effect on these types of films. To use them for neutron imaging one needs to introduce a suitable neutron converter just before the film. Charge particles are generated through recoil mechanism in the converter and these charge particles expose the film which is later processed. Direct and transfer techniques using metal converter foils and track-etch technique using X-ray film and nitro-cellulose film respectively are in general used for neutron radiography purposes. Neutron-based imaging using films is a two-step process. In the first step, specific thin foils (thickness ~ 125 μm) are activated spatially as per the un-attenuated neutron intensity by the neutrons passing through a sample. In the next step, they are taken out from irradiation site, kept in contact with an imaging film to get exposed from the decay radiation (beta rays) from the foil. The film is then developed as carried out in auto-radiography technique. The film then can be scanned for processing and archiving in digital format. The active component of a film comprises of an emulsion of radiation-sensitive materials (silver halide crystals suspended in gelatin) coated onto a transparent base material. One of the most important characteristics of film is its sensitivity, termed as film speed. This parameter determines the amount of exposure required to produce an image. A film with high sensitivity or speed requires less exposure than a film having lower sensitivity or speed. Another important parameter of film is its optical density and it is the quantification of the amount of light penetrating the film. Interested readers may delve into the book, “The photographic process and Film Sensitivity” by Perry Sprawls. In case of thermal neutron imaging, Dysprosium (Dy) and in case of epithermal neutron imaging, Indium (In) foil is used as the primary neutron detector. Shaikh [39] has described the use of Indium foils in his hydrogen sensitive epithermal neutron (HYSEN) radiography work. The imaging was carried out by placing the object in between a neutron beam filter comprising of 1 mm Cd and In foils and the imager consisting of 250 μm Indium converter screen. The filter efficiently gets rid of neutrons below 1.49 eV. They are chosen for their high neutron cross-section with the neutrons of the specific energy range. The beta energies for Dy and In foils are 1.28 and 1 MeV (Mega electron Volt), respectively. They are also developed far away from the irradiated site in order to get rid of gamma background-related issues. Though the transfer technique is time-consuming, but provides high-quality radiographic images. The transfer of image from the activated foils can also be taken by using Image Plate and then reading out through image plate scanner. In this case, the film processing is not required and the scanned image is available in digital format. This type of imaging with neutron sensitive image plate is known as neutron computed radiography or nCR. Detailed discussion on image plate is carried out in the next section.

3.6.2 Neutron Image Plate (NIP)

X-ray image plates are extensively used in X-ray diffraction and related studies in basic sciences and also for projection imaging in medical imaging techniques known as computed radiography. Combining thermal neutron convertors (B, Li, Gd) with these devices can make them employable towards neutron imaging applications providing resolution ~ 0.1–0.2 mm. Comparison between film and IP are provided in Table 3.3.

Definition: IPs are flexible film-like imager devices having specific phosphors to trap radiation energy and store for deciphering the data using laser-based scanning

Table 3.3 Comparison of some salient features of film and IP

	Film	Image plate
Sensitivity	High	Ultra high (1–2 order higher than film)
Dynamic range	10^2	10^4–10^5
Linearity	Good	Good
Intrinsic spatial resolution	High	Less than film
Reusability	No	Yes
Ease of use	No, elaborate developing mechanism involved	Yes, irradiate—scan—erase—use

method. The phosphors have special properties that utilize photo stimulated stimulation phenomena (PSL) which is different from phosphoresce and fluorescence. When these phosphorous are irradiated by radiation, say UV, X-ray, charge particles, neutron they produce colour centers where electrons get trapped. In other terms, we can say that proportional to the variation in un-attenuated neutron radiation, from the sample, is stored in the plate. When a PSL excitation light suitable for the absorption spectra of the colour center is irradiated, the trapped electron are liberated, producing luminescence and collected by a photo detector. The scanned data is registered in spatially resolved locations in a 2D format and an image is generated. The pitch by which the image plate is scanned, provides the resolution of the image, though it is not the actual resolution of the image plate. The finer the pitch, the higher the scanning time and larger is the size of the image. After scanning the IP can be erased of any background or trapped electron through UV irradiation and made ready to be used again.

Since the IPs are also sensitive to Beta, X-ray, gamma and alpha, for neutron imaging applications, the plates are positioned inside specially designed cassette having a lead sheet for gamma shielding. An important point to note is that the timing gap between the end of exposure and the start of readout should be minimized to get rid of fading phenomena. After exposure to radiation, the electrons are locked in metastable state. They are then stimulated by red light during the scanning process and they emit photostimulable luminescence. But due to thermal influence, some of them can de-excite and hence cause fading. Two types of scanners are available, flat IP type and curved IP type, though the mechanism of scanning and data readout is the same.

The basic construction of an IP for thermal neutron imaging is composed of the two admixtures coated on flexible support. The admixtures are of fine particles of (BaF(Br/I):Eu) and suitable neutron convertors such as nat Gd_2O_3 or nat LiF [40]. This mixture of photostimulated luminescence material forms the intrinsic part of the neutron IP. When using Gd_2O_3 as neutron converter, the stoichiometric ratio of Ba and Gd atoms is 1:1 in the substrate. Depending upon the requirement of detecting efficiency and spatial resolution, the intrinsic part thickness is decided. Their size can be as large as 40 cm * 46 cm. The main advantages of NIP's are short exposure time and broad dynamic range. The scanned image can have 16 bit data range which can help in revealing very low contrasts. The main disadvantages with NIP's are that they are not suitable for real-time imaging as well as tomographic applications and time-consuming processes. As an example, high-resolution scanning (~50 μm) of a 20 cm × 20 cm NIP can take 30 min. These types of NIP's are also used for cold neutron radiography and tomography applications.

FLA-9000 Starion by Fujifilm Life Science USA [41], as shown in Fig. 3.13, is commercially available Fujifilm's flagship image scanner. The FLA-9000 is capable of radioisotopic, fluorescent, chemiluminescent, and digitized imaging applications. It is a multipurpose image scanner designed to perform a variety of proteomic research applications. The scanner can accommodate up to four of a possible five lasers (473, 532, 635, 685, and 785 nm) at once. Three different models support a variety of your imaging needs:

Fig. 3.13 Photograph of FLA-9000 Starion by Fujifilm Life Science USA (downloaded from https://www.selectscience.net/products/fla-9000-starion/?prodID=84313#tab-2, accessed date 11/05/2021)

- IP Model: ideal for phosphor imaging
- RGB Model: ideal for multi-spectral 2D gel imaging
- IR + IP Model: ideal for conducting near-infrared and radioisotope imaging.

Commercially available neutron image plates (C-NIP) having mixture of BaFX:Eu^{2+} (X = Br, I) and Gd_2O_3 are an excellent choice but they are also sensitive to gamma radiation which are always present in neutron-based experiments. New developments in this direction towards reducing gamma sensitivity has been carried out M Schlapp and co-workers of Germany, initial idea provided by Masalovich and Laffe [42], by fabricating ceramic image plates consisting of KCl:Eu^{2+} and LiF. The drawback of this type of scintillator is the reduced absorption cross-section of LiF compared to Gd_2O_3 (940 barns for enriched ^{6}Li and 48,890 barns for ^{nat}Gd) for thermal neutrons and hence thicker version is required and this invariable results in loss in spatial resolution. This drawback can be overcome by structuring honeycomb-type cells in the ceramic and embedding in the image plate. Due to its design, they are named as Pix-NIP [43]. This novel technique allows read-out from particular illuminated cells during scanning procedure. Experimental results suggest that the Pix-NIP provides higher contrast transfer from original image to the detected signal compared to C-NIP. Typical resolution values at 20% MTF are 680 µm for C-NIP and 570 µm for Pix-NIP. The increase in resolution may be attributed to the confinement of light into individual pixels in the case of Pix-NIP. An important drawback of this Pix-NIP is that their resolution is dependent on the honeycomb structure. Moreover, NIP's based on KCl:Eu^{2+} are still brittle and lots of developments are to be carried out. For fast neutron imaging copper and polyethylene sheets [44] are used as fast neutron converters. The charge particles generated in the converters cast image on the IP and later on read through scanners.

3.6.3 Scintillator-Based Detectors

Neutron detection is driven by the methodology of using composition of materials which upon interaction with neutrons provide charge particles or ions and these then deposit their energy to provide signals to be detected by suitable detectors. Since fast neutrons interact weakly with all materials in comparison to thermal neutrons, for detection of fast neutrons they need to be moderated to some extent to thermal or near thermal range to make their interaction viable and hence detectable.

3.6.3.1 Polycrystalline-Based Scintillators

(A) **Thermal neutron scintillators**: The development of scintillator-based thermal neutron detector was driven by the large interaction cross-section with 6Li, 10B and Gd. These sort of materials (in powder form) are mixed with ZnS(Ag) and fabricated as screens for area imaging purposes. A point to note is that for detection purposes the scintillator thickness must be high, within the limit that it does no stop its own emission to reach the photo detector, as one needs to stop maximum number of neutrons as spatial resolution issue is of no importance. But in case of imaging, spatial resolution matters and for this purpose there is a trade-off between the thickness of scintillator and the amount of radiation to be stopped or in other terms the detection efficiency. Out of these ^{6}LiF-ZnS(Ag) and Gd_2O_3S are the most used scintillator due to their high efficiency. The basic interaction of Li and thermal neutron is given by $^6\mathrm{Li} + \mathrm{n} \rightarrow {}^3\mathrm{H} + \alpha$ (Q: 4.78 MeV). The energy of the triton and the alpha particles are $E_{3H} = 2.73$ MeV, $E_\alpha = 2.05$ MeV, respectively. Thickness of such scintillators ranges between 0.3 and 0.6 mm. For example, ^{6}LiF-ZnS(Ag) based scintilator screen has been developed by Eljen Technologies. The enrichment of ^{6}Li is ~ 95%. [35]. With the ^{6}LiF: ZnS mass ratio of 1:2 the theoretical and experimental thermal neutron detection efficiency reported is 36 and 32.4% respectively [45]. The light yield of its surface at the average value of the charge spectrum was approximately 8000 photons/neutron. They are very poor towards gamma sensitivity. Commercially, named as EJ-426, they are available with various options such as clear polyester sheet, aluminized mylar, pure aluminum, or highly reflective aluminum and chosen as per the application need. These scintillators have been under use for more than 4 decades and up-gradations (in terms of optimization of weight ratios of elements in the mixture) towards betterment in sensitivity, increase in light production, and image resolution. RC Tritec AG developed scintillators such as ^{6}LiF/ZnS:Cu, ^{6}LiF/ZnS:Ag and ^{6}LiF/Zn(Cd)S:Ag having thickness ranging from 50 to 400 μm are commercially available. Other than in sheet form, cerium activated lithium silicate glass scintillators are also used for thermal neutron radiography. In the upgraded Neutron Radiography Facility (INDLOVU) at the SAFARI-1 Research Reactor in South Africa scintillator materials such as 0.05 mm or 0.10 mm thick ZnS:Cu/6-LiF screens, a 0.01 mm thick (GADOX) Gd2O2S:Tb/6LiF: 80/20 screen and a 1.5 mm thick PP30 (30% ZnS:Cu) converter have been used depending upon the intended application [46].

Work in this direction are constantly progressing towards image quality improvement such as using micro-particles of ^{6}LiF and coating it with ZnS(Ag) [47]. Development of high-resolution high-efficiency micro-columnar LiI screens for thermal neutron imaging has been reported [48] by Radiation Monitoring Devices, Inc., Watertown, MA, USA. Feasibility studies on ^{6}Li loaded plastic scintillation films have been carried out by researchers [49] at the University of Tennessee, Knoxville, TN, USA. Screens based on ^{6}Li-enriched silicate glass cores with Ce activator have shown promising results for thermal neutron imaging. Commercial Li-glass scintillators for neutron detection and imaging are available from Scintacor [50].

Another detector known as scintillating fiber (SCIFI) based neutron imager has been reported by Michael Edward Moore [51] of University of Tennesse, Knoxville. Thermal neutrons interacting with ^{6}Li-doped optical multicore SCIFI produces charge particles which in turn produce primary and secondary electrons in the Li silicate glass matrix. These then interact with the Ce activator and provide enough scintillation to be guided to any suitable optical imaging detector through the microstructured waveguides.

GOS or Gd_2O_3S(Tb) based scintillators also have proven a candidate for thermal neutron imaging. The guiding interactions are

$^{155}\mathrm{Gd} + \mathrm{n} \rightarrow {}^{155}\mathrm{Gd} + \gamma$ (0.09, 0.20, 0.30 keV) + conversion electrons; ($\sigma_{\mathrm{th}}\ n =$ 61,000 b)

$^{157}\mathrm{Gd} + \mathrm{n} \rightarrow {}^{158}\mathrm{Gd} + \gamma$ (0.08, 0.18, 0.28 keV) + conversion electrons; ($\sigma_{\mathrm{th}}\ n =$ 255,000 b)

The abundance of ^{157}Gd in natural Gd is 15.7%. The efficiency can be increased manyfold if this isotope can be enriched. With ~ 88% enrichment of $^{157}Gd_2O_3$, 3.8 and 3.6 factor of increase in absorption power and light yield with respect to its natural counterpart has been reported by researchers at Paul Scherer Institute (PSI), Switzerland [52]. RC Tritec AG [53] developed scintillator screen $^6LiF/Gd_2O_2S$:Tb provides 30–50% increase in brightness for the same resolution in comparison to Gd_2O_2S:Tb for neutron imaging. The emission is in the blue-green region and well suited for effective coupling with commercially available high-resolution CCD camera for imaging purposes.

Thermal neutron interaction with B-10 is as follows.

$$^{10}\mathrm{B} + \mathrm{n} \rightarrow {}^{7}\,\mathrm{Li} + \alpha + \gamma(0.48\ \mathrm{MeV})(\mathrm{Q}{:}\,2.31\ \mathrm{MeV})$$

The thermal neutron capture cross-section of B-10 is 4 times that of the Li-6. This certainly suggests that the scintillator screen containing B-10 will provide more detection efficiency than the Li-6 based ones. Though Gd has higher thermal neutron capture cross-section than B-10, it is sensitive to gamma and that is not the case with B-10. Also, the daughter products generated in case of thermal neutron interaction with boron have less energy and larger size than the daughter products with the case for Li and Gd. This has direct relation to the light spread on energy deposition; less energy and larger size means less travel in the base material and hence better spatial resolution. Because of these reasons, boron-10 based scintillators can provide higher performance than Li- or Gd-based scintillators for thermal neutron imaging even though they have lesser light output comparatively. RC Tritec AG developed B-10 based scintillators such as $^{10}B_2O_3$/ZnS:Cu, $^{10}B_2O_3$/ZnS:Ag and $^{10}B_2O_3$/Zn(Cd)S:Ag having thickness ranging from 50 to 400 μm are available. They are capable of providing high light output and high-resolution thermal neutron radiography images [53].

Study involving 25 different boron-based scintillators towards comparison with commercially available LiF and Gd-based scintillator screens and the parameters for the best image quality has been carried out by William Chuirazzi and his co-workers. It was found out that thinner boron-based scintillators could provide similar detection efficiency and better spatial resolution in comparison to ^{6}LiF-based scintillators. Interested readers may please go through the article [54].

Studies involving Dysprosium-based scintillator screens, fabricated by depositing mixtures of ZnS:Cu scintillator with Dy_2O_3 (in varied mixing ratios and grain sizes of ZnS:Cu) in Aluminum plate and Dysprosium foils have been reported. The isotope ^{164}Dy (28.18% of natural Dy) is useful in neutron imaging as its absorption cross-section is ~ 1000 b. Experiments at NEUTRA beamline (PSI) [55] suggests that the highest light output was provided by the screen having Dy foil as substrate and mixing ratio of 1:2 of Dy_2O_3: ZnS:Cu (grain size 9.67 μm). Though their spatial resolution was slightly poor than the standard ^{6}LiF:ZnS scintillator screen they are having much less sensitive to gamma radiation and have potential use in neutron imaging of irradiated fuels. The latent image created on the Dy foils by the neutrons crossing the sample can be read by a well-shielded sensitive CCD camera system kept at a distance from the actual neutron beam port.

Boron-rich Multi-Channel Plate (MCP) based imaging detectors [56, 57] have also been used. The neutron interacting with the boron coated on the inner walls of the MCP produce charge particles which then release secondary electrons. These are then multiplied in the MCP are read-out through specialized sensors and electronics. The best part of this type of detector is the high resolution provided by the MCP size (~10 μm) and the dedicated electronics for fast read-out and processing. But their drawback lies in their low efficiency (10–39% for thermal neutrons). Using neutron sensitive MCPs coupled to a Medipix2/Timepix active pixel sensor [58], feasibility experiments at both thermal as well as cold neutron beamlines at PSI established neutron imaging having spatial resolution ~ 55 μm. “Medipix2” [59] is a type of hybrid detector initially developed for charge particle detection with high temporal resolution for CERN experiments but various modifications have led to their use for applications including medical imaging, neutron imaging [60] etc. Basically, it is a semiconductor detector chip having pixelated matrix in the front and a common readout on the backside. Each pixel element has its own readout mechanism through individual preamplifier, discriminator and digital counter.

As an alternative to the abovementioned scintillator, ($H_3\,^{10}BO_3$) in combination with ZnS(Ag) having mass ratio of 1:6 has shown potential in thermal neutron imaging applications [61]. It has been characterized at the d-Be neutron source facility at Peking University of China. The best performance with 0.35 mm thick scintillator was found out to be approximately 1.33 lp/mm (line pair per mm).

Another notable development in this field is the development of a thermal neutron imaging screen consisting of a pixelated microstructured CsI(Tl) sandwiched between two GdF_3 layers [62]. Thermal neutron interaction with Gd atoms produce conversion electrons which in turn produce scintillations in CsI(Tl). In this regard, aluminum-based substrates were found to be better than fibre-optic plate substrates in terms of light output, signal-to-noise ratio and contrast as per imaging tests at a thermal neutron port of the University of Massachusetts Lowell Research Reactor (UMLRR). One of the reasons for this can be attributed to the columnar structure of the CsI as well as the high absorption coefficient of Gd.

(B) **Fast neutron Scintillators**: Detection and imaging of fast neutron have always been a challenge. To achieve this, one need to slow down the fast neutron to energies where they interact through neutron-induced nuclear reaction to generate charge particles which then produce scintillations in accordance with the phosphor as detectable luminescent signals. As the number of collisions required to slow down the fast neutrons to make it compatible to (n, p) reaction, their thicknesses are more than the thermal neutron scintillators. For this very reason, the spatial resolution as well as contrast obtained in fast neutron radiography (FNR) is poor than Thermal Neutron radiography (TNR). The light signal can now be coupled with a CCD camera, amorphous Si panels or suitable semiconductor screens. Since the light output is very poor, when coupled with lens and CCD-based imaging components, the acquisition time goes very high. It becomes very time intensive in case of tomography experiments.

(C) **Plastic Scintillator (PS)**: PSs are compound formed by solid solutions formed by solid solution of organic scintillation materials in polymerized solvent. Owing to their physical properties, they can be easily molded and fabricated in any desired shape. These make them extremely useful towards development of organic scintillation-based detectors. Since these materials are of low Z, their gamma sensitivity is poor and effective toward charge particle detection with fast timing response. Fast neutron-induced (n, p) reaction generated protons directly or through further ionization deposit their energy in the matrix. Though the emission wavelength depends upon the organic activator present in the matrix, in general, the emission peaks around 400 nm.

As for example, Saint Gobain makes plastic scintillator (Trade name BC412, BC416) used for fast neutron imaging has light output and wavelength emission of anthtracene are (60% for BC412 and 38% for BC416) and 434 nm respectively. Saint-Gobain [63] (erstwhile Bicron), USA commercially also produces a scintillator in the trade name of BC 720 ZnS(Ag) for fast neutron detection. Using such pixelated scintillators and coupling to photo-detectors area imaging can be performed.

Thick transparent plastic scintillators (10–40 mm) have been successfully used for imaging with neutron (1–14 meV). High energy 10 meV neutron imaging has been successfully carried out at the LLNL, USA by imaging systems comprising of BC 408 and BC 400 scintillators (developed by Saint Gobain) and a compatible lens coupled CCD camera detector [64]. The schematic of a typical high-energy neutron imaging setup is shown in Fig. 3.14.

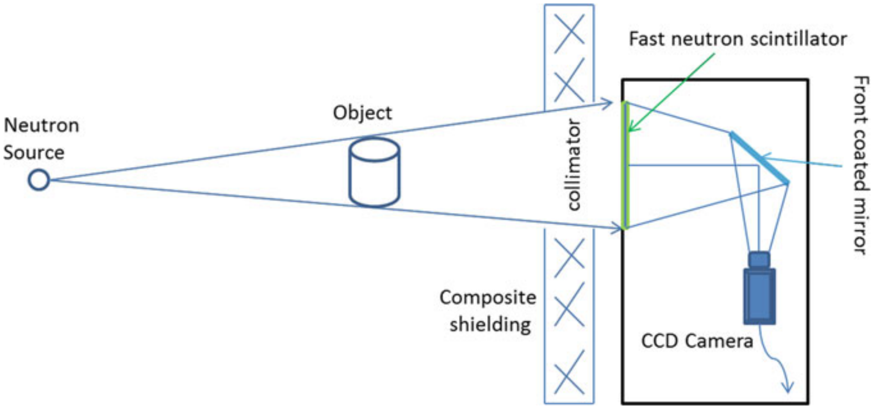

Fig. 3.14 Schematics of a typical high-energy neutron imaging setup

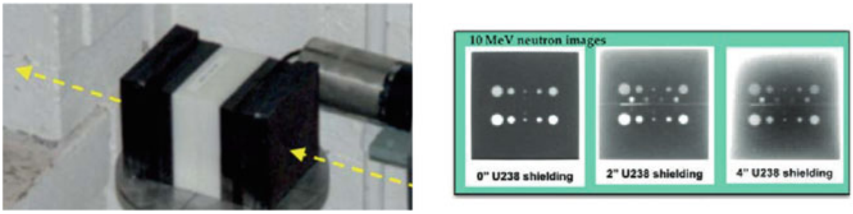

Fig. 3.15 (left) photograph of the test piece comprising of plastic piece sandwiched between DU with holes and (right (top) 10 MeV neutron radiographs with varying DU thickness (reproduced from Ref. [65] with permission from Rightslink by CCC)

Figure 3.15 shows the test sample, plastic piece sandwiched between depleted uranium (DU) blocks having holes of various diameters and its 10 MeV neutron radiograph at the Ohio University Accelerator Lab (OUAL) using an imaging system consisting of BC-408 scintillator, a turning mirror and a cooled CCD camera [65]. It is seen from the neutron radiographs could reproduce the holes clearly though the ability reduces with increase in DU thickness.

Researchers of Swiss Federal Institute of technology and PSI Switzerland has reported the development of a novel fast neutron detector system for tomography purpose using DD neutrons [66]. The primary component of the detector is aluminum mylar wrapped BC400 plastic and in the form of an array of 88 detectors. Each detector's dimension was 80 mm deep (In line with neutron path), 8 mm height and 5 mm wide (Perpendicular to the neutron path and parallel to the ground). Since individual detector represents a pixel, their response and output need to be normalized for imaging application. The achieved spatial resolution by the group was reported 2 mm, the scintillator output read by SIPMs connected to Multichannel DAQs and digitizer. The current in each channel is digitized to provide a grey value corresponding to a pixel in the 2D plane. The photograph of the detector assembly is shown in Fig. 3.16.

Feasibility experiments on fast neutron imaging using 14 MeV neutrons from DT neutron generator and 40 mm thick BC400 plastic scintillator and a EMCCD (Electron Multiplying CCD) camera have been demonstrated at BARC, India [67]. Fast neutron radiography images of step wedge samples of HDPE, MS and Pb with their intensity profile across the steps are shown in Fig. 3.17.

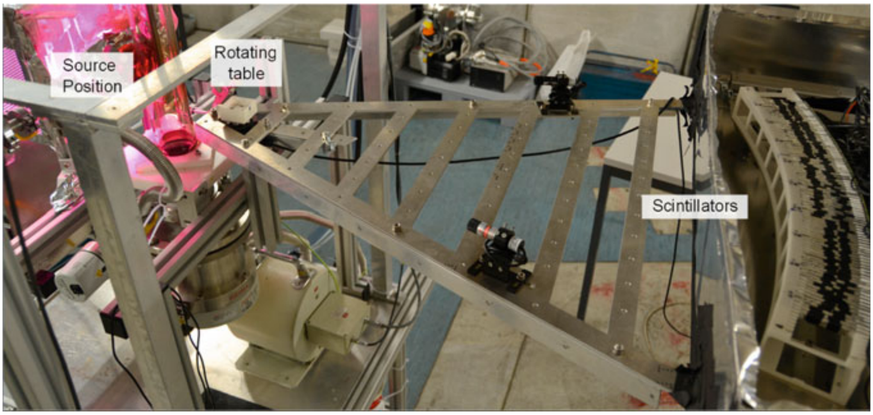

Fig. 3.16 Photograph of the source, rotating table and detector array (with scintillators) at the PSI, Switzerland (reproduced from Ref. [66] with permission from Rightslink by CCC)

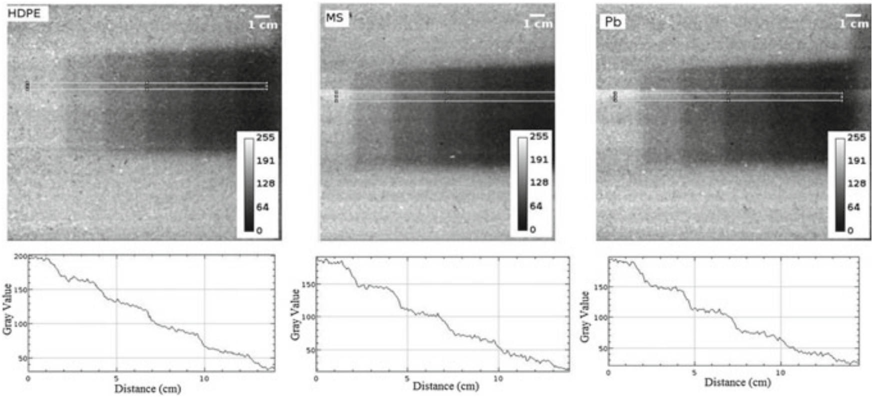

Fig. 3.17 Fast neutron radiography images of step wedge sample of (left) HDPE (middle) MS and (right) Pb with their intensity profile across the steps. The step wedge sample size is 50 mm × 100 mm × 20–100 mm [width (w) × height (h) × depth (d)] with 20 mm step height. The fast neutron imaging system at BARC, India has been upgraded by using a 3 mm PP-ZnS(Ag) fast neutron scintillator screen and an image intensified CCD camera (reproduced from Ref. [67] with permission from Rightslink by CCC)

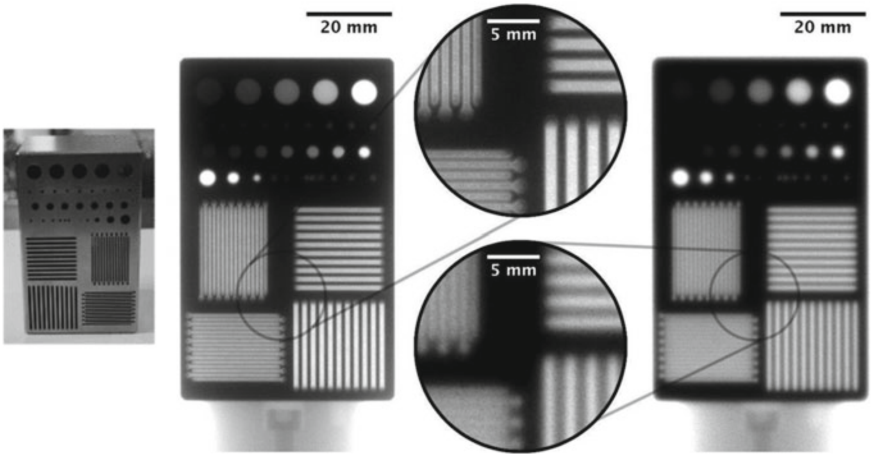

Fig. 3.18 Radiography of an iron block (shown on the right) having different diameter holes and slits along its thickness imaged with the 2 different scintillator types. Left with the 2 layer PE (3 mm)/ZnS:Ag (60 μm) and right with the standard 2.4 mm PP/ZnS:Cu (30%) scintillator at the NECTAR facility at FRM-II research reactor, MLZ, Garching (reproduced from Ref. [68] with permission from Rightslink by CCC)

Development of ZnS mixed in polypropylene base has been reported and also commercially available by RC Tritec AG (rctritec.com). This type of scintillator has been used for imaging with fast neutrons at the NECTAR facility located at FRM-II nuclear research reactor. Two variants tested with NECTAR facility are PP/ZnS (As) (Emission wavelength 450 nm) and PP/ZnS(Cu) (Emission wavelength 530 nm). They are available in thickness ranging from 1–5 mm. Figure 3.18 displays the radiograph of an iron block having different diameter holes and slits along its thickness imaged with the 2 different scintillator types, namely 2 layer PE (3 mm)/ZnS:Ag (60 μm) and 2.4 mm PP/ZnS:Cu (30%) at the NECTAR facility at FRM-II research reactor, MLZ.

(D) **Fibre Scintillator screen**: These screens are composed of polystyrene fibres arranged in 2D fashion on a PMMA base. The fibers are doped with fluorescent materials as per the radiation to be detected. At Lawrence Livermore National Laboratory, Livermore CA, the fast neutron imager consists of a 160-mm × 160-mm × 50-mm thick array of 250-μm round BCF-99-55 scintillating fiber, manufactured by Saint Gobain. In the lens coupled option the spatial resolution of the system is 5.5 lp/mm. This sort of system in combination [69] with a specially designed neutron pinhole aperture array was used at the National Ignition Facility, for imaging of size and shape of DT plasma emitting neutrons during the ignition phase. In order to increase the spatial resolution, some of the recommendations are as follows: development of liquid capillary array for use with liquid scintillators, high index fast liquid scintillator and improving quality of optical fiber arrays [70].

3.6.3.2 Single Crystal-Based Scintillators for Thermal Neutron Imaging

Rare earth based single crystal based scintillators are being used in various applications including healthcare imaging using X-rays for a long time. Gas detectors based on ^{3}He and ^{10}B provides very high detection efficiency owing to their high absorption cross-section. But the dwindling supply of ^{3}He gas has motivated researchers to look for promising candidates for neutron detection. Though inorganic scintillators are widely used for neutron imaging the light output spread in them, which depends upon the grain size of the converter material and substrate thickness, restricts their spatial resolution and contrast. Rare earth scintillators based on Ce-doped Li glass and Eu^{2+} doped LiI have shown neutron detection capabilities [71] but the former one has gamma sensitivity and the later one is highly hygroscopic. Crystal in solid form is supposed to increase detection efficiency because of their structure or in other terms higher atomic density of neutron capture atoms, if present, increases the interaction probability. Moreover, if it is single crystal, then the light spread will be minimal. Both these properties are the motivating factors for the development of single-crystal scintillators as a thin crystal (< 1 mm) can stop all thermal neutrons falling on it.

Some notable developments in this category of scintillators are discussed below:

A two-inch diameter and 2 mm thick wafer of Eu (2 mol %) doped $LiCaAlF_6$ (95% enriched ^{6}Li) developed by μPD (micro pulling down) technique in combination with a position-sensitive PMT has been reported for use in thermal neutron imaging providing spatial resolution better than 1 mm. Thermal neutron interacting with Li atoms produce α particles and these interactions with Eu^{2+} result in an emission peaking at 375 nm. Lots of research has gone into the understanding of the doping percentage, light emission dependence, etc. towards this development [72–75]. Experiments were carried out at the MUSASI (Multi-Purpose Thermal Neutron application and Science) beam port in JRR-3 (Japan Research Reactor-3). Test pieces made up of 1 mm thick cadmium plate having holes of diameter 1, 2, 3 and 5 mm and a complicated object made with 1 mm diameter cadmium wire were imaged (as shown in Fig. 3.19) with clarity. This crystal has also shown an order less scintillation under gamma radiations. Though the effective imaging area was small yet this work has proved the use of single-crystal neutron scintillators for thermal neutron imaging.

Ce-doped $Gd_3Ga_3Al_2O_{12}$ (GGAG:Ce) single crystal has been developed by Czochralski method at BARC, India and its study related to thermal neutron detection and imaging [76] has shown promising results. Gd atoms have the highest capture cross-section and a thin slice (< 1 mm) of GGAG:Ce can have almost 100% stopping power for thermal neutrons, which is directly related to the detection efficiency. Thermal neutron interaction with Gd atoms produces gamma and conversion electrons which are continuous upto 8.5 MeV. These excite Ce atoms (Ce^{3+}–5d-4f transitions) and the scintillations are recorded by a suitable photo detector. A 1 mm thin slice, cut from the ingot, was polished to a final thickness of 0.55 mm (Fig. 3.20a).

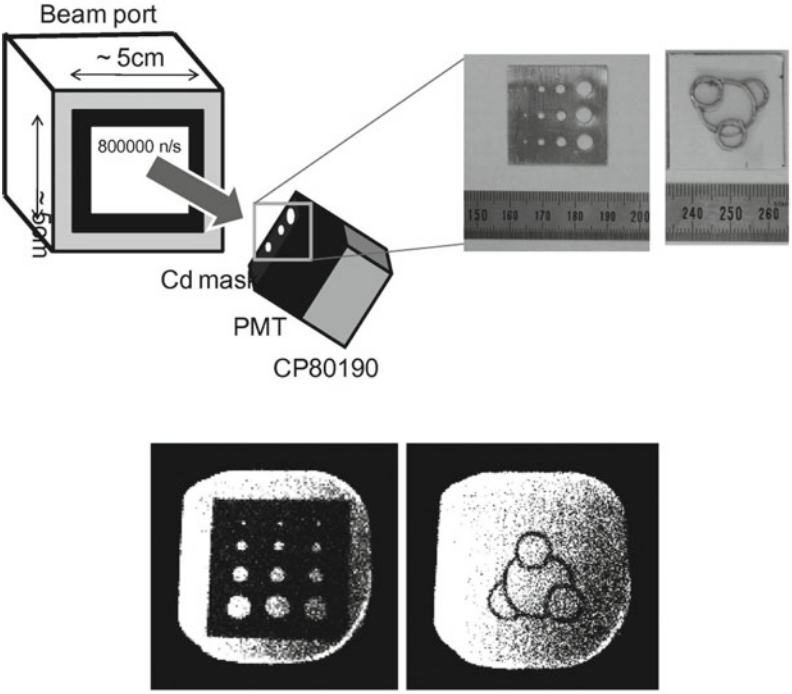

Fig. 3.19 (top) schematic drawing of the experimental setup and the test pieces imaged, (bottom) thermal neutron radiographs of the test pieces (reproduced from Ref. [73] with permission from Rightslink by CCC)

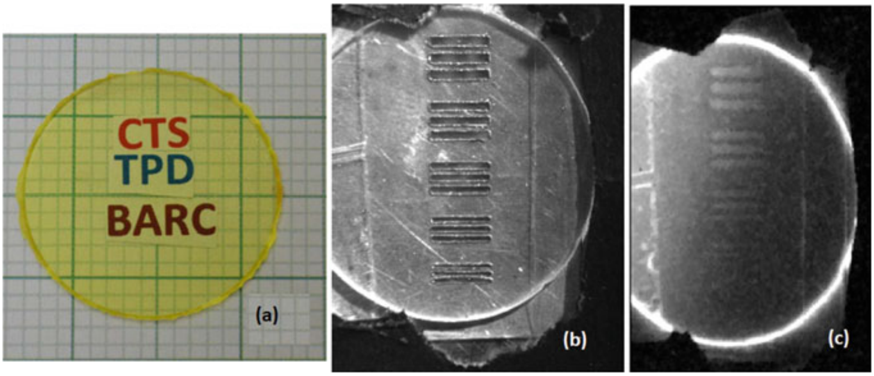

Fig. 3.20 **a** photograph of Ce-doped $Gd_3Ga_3Al_2O_{12}$ single crystal developed at BARC, India, **b** optical image showing the cadmium slits of varying dimension (0.5–4 mm) and **c** the thermal neutron image revealing the cadmium slits (reproduced from Ref. [76] with permission from Rightslink by CCC)

After characterization, its feasibility was tested at the thermal neutron imaging beamline at Dhruva reactor, BARC. Since its peak emission is around 550 nm, its coupling to CCD camera with lens was easily achieved. A portable neutron imaging system comprising of 0.55 mm thin GGAG: Ce crystal, a 90^0 turning mirror and off-the-shelf available Manta make CCD camera was developed. A mask made of Cd plate (1 mm thick having 0.5, 1, 2, 3 and 4 mm) was imaged. The optical and the thermal neutron image of the cadmium slit is shown in Fig. 3.20b, c respectively.

3.6.3.3 Semiconductor Based Detectors

(A) **Flat panel based detector**: In the same line of development of X-ray flat panel detector using amorphous silicon panels, coupling a neutron scintillator in place of X-ray sensitive screen, will give a neutron sensitive amorphous flat panel. As discussed above CCD camera based imaging systems using ^{6}LiF scintillator use lens coupling. This introduces some loss in the light collection which is already poor in intensity. This is not the case with flat panels as the scintillator screen is directly bonded with the panel [77] and hence they provide better light collection efficiency. They can be of large size but the cost increases sharply with size. The main drawback of these detectors is that in general their dynamic range is poor (14 bit) than CCD cameras (generally 16 bit), and 16 bit flat panels are very costly.

(B) **Semiconductor detector**: Complementary Metal Oxide Semiconductor (CMOS) devices gained attention over charge coupled devices (CCD) after the advancement of lithography technology as smaller pixel sizes could be realized incorporating the achievable fill factor. They have added advantage of low power consumption and fabrication of large panels using tiling mechanisms. With X-ray scintillating screens in their input side, they become X-ray imaging detectors. One such pixelated X-ray detector is PILATUS [78]. Researchers at the PSI have developed a neutron imager using PILATUS-II using Gd-157 as neutron converter. In the same line of development, using converter materials such as B-10, Li-6 and Gd incorporating on a new pixelated readout chip named EIGER (Enhanced Intensity and Greater Energy range) has been developed at PSI. EIGER, a hybrid detector with single photon counting capability, has been initially developed by PSI-SLS group for applications at Swiss Light Source. In Pilatus-II, 5 μm Gd layer was bump bonded using Indium to the chip. Initial results at the NEUTRA, PSI has provided encouraging results and improved its performance by removing issues such as edge smearing is being worked out. Also, the sensitivity of Gd with X-ray/gamma does pose some restrictions of their use for practical applications.

3.6.4 Gas-Based Detectors

Thermal neutron detection capability of Helium-3 and Boron-based gas detectors are well established. These gases have high absorption cross-section (He-3: 5840 barns; B-10: 3500 barns) for thermal neutrons. These detectors are in general cylindrical having diameter ~ cms and length ~ 10's of cms. Though they are routinely used for neutron dose and flux monitoring purposes.

He-3/BF_3 based neutron detectors:

These sort of gas-filled detectors were the first devices used for neutron detection and they work in the proportional region. They are in general housed in Aluminum or stainless steel cylinders with electrical connector at one end. Thermal neutrons entering the detector ionize the respective gas atoms, generate charge particles (positive ions and electrons) which then are collected and signal is generated. This happens only when designated positive potential is applied to the detector, otherwise the charge particles are lost due to recombination in the gas medium. The generated signal is processed further with nuclear instruments such as pre-amplifier, single channel analyzer, counter, etc. The interaction equations for both the gases with thermal neutrons are given below.

$$^3\mathrm{He} + \mathrm{n} \rightarrow ^3\mathrm{H} + \mathrm{p}(\mathrm{Q}\text{: } 0.764\,\mathrm{MeV})$$

The energies of the triton and proton are 0.191 meV and 0.573 meV respectively

$$^{10}\mathrm{B} + \mathrm{n} \rightarrow ^7\mathrm{Li} + \alpha + \gamma(0.48\,\mathrm{MeV})(\mathrm{Q}\text{: } 2.31\,\mathrm{MeV})$$

The energy of Li ranges from 0.84 to 1.01 meV and that of α ranges from 1.47 to 1.78 meV. In case where high detection efficiency is required, He-3 detector is preferred over BF_3 detectors as in the former case they can be operated at much higher pressures thereby enhancing gas multiplication and in turn more signal output. But in situation where gamma environment is very high, BF_3 are favoured over ^{3}He detectors. In cases where the neutron flux environment is very high, the internal walls are coated with activated charcoal which reduces the effect of output pulse reduction due to generation of electronegative gasses during irradiation. Some additive gas such as CO_2 or Ar are also put in these detectors to minimize γ-ray pile up by modifying the speed of electrons and thereby allowing use of fast processing electronics. The operating voltages for these gas detectors lie between 700 and 1000 V, off-course it also depends upon the construction and intended application. These detectors are routinely used in neutron facilities for area dose measurement, flux mapping etc. Since the active volume of interaction is ~ 10's of centimeters, they cannot provide spatially resolved information better than their size.

Gas-based detectors with oxide film coating of fissionable elements such as U235 or Pu239 on the inner surface of the cylinder can also be utilized for thermal neutron detection. They are called fission chambers. The thermal neutrons cause fission upon interacting with the fissile material and generates fission fragments which also include

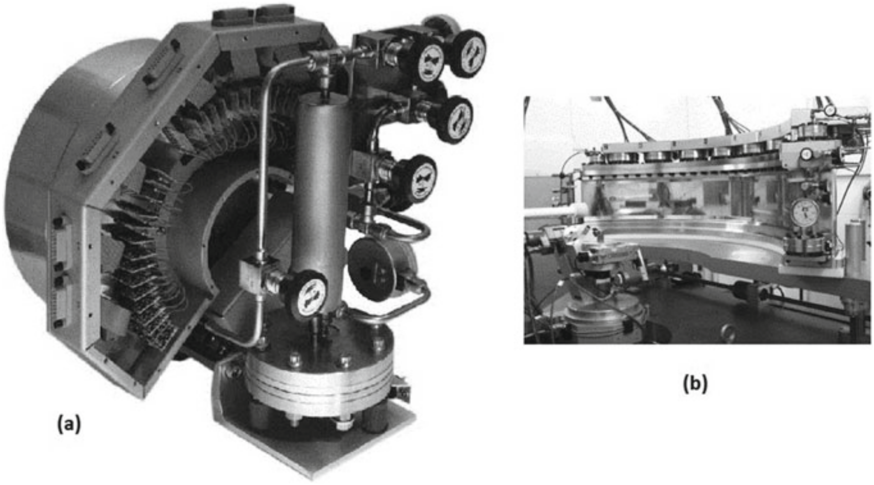

Fig. 3.21 **a** (left) Photograph of a 2D neutron detector based on multiwire chamber filled with He-3 developed at BNL and **b** complete detector set comprising of multiple segments installed on the goniometer on the Protein Crystallography Station (PCS) at Los Alamos (reproduced from Ref. [79] with permission from Rightslink by CCC)

charge particles. The rest of the process of signal generation is the same as discussed above. They are mostly used for reactor monitoring purposes.

Though the abovementioned detectors are highly efficient and robust in nature, they are directly not suited, in the present configuration, for area imaging applications.

In this direction, initial work towards development of area-imaging detector primarily on multi-wire chamber design but filled with He-3 gas mixture was carried out for studies of molecular biology and material science applications [79]. Figure 3.21 shows the photograph of the developed 2D detector with 5 cm × 5 cm sensitive area in (a) and neutron detector with 120° × 15° angular coverage on a radius of curvature of 70 cm in (b).

Researchers at BNL in collaboration with ANSTO has developed and tested a 1 m * 1 m (active area 0.96 m * 0.96 m), 3He based gas detector [80] where the generated signal is collected by discrete anode pads located in 2D separated by pitch. The signals are read by the low noise ASICs. The detector is kept inside a vacuum tank to reduce scattering of neutron and cooled to reduce noise in the electronics.

Development of the 2D neutron detection with an effective size of 200 mm*200 mm having ^{3}He gas and working on MWPC methodology has been reported [81]. Cathode and anode planes are composed of aluminum foil and gold plated tungsten wire respectively. The signals generated at specific (x, y) coordinates/positions are read out by electronic modules. The best positron resolution achieved using the detector is 1.18 mm.

BioRef is the standard versatile novel time-of-flight instrument developed at Helmholtz-Zentrum Berlin for applications [82, 83] on soft matter systems. It is a 30 cm × 30 cm active area 2D position-sensitive detector based on ^{3}He multi-wire chamber and delay line electronics. In comparison to CCD based imaging where the resolution is ~ 25 μm the spatial resolution of this detector is 2 × 3 mm^2. But, because of ^{3}He its detection efficiency is superior for cold neutrons and also provides time resolution ~ μs, this instrument is best suited for TOF measurements. Experiment on strain measurements on a flat steel sample under tensile loading has been reported by Strobl et al. using this instrument.

In the detection and imaging with neutrons (40–400 meV), a proof of principle experiments was successfully carried out in 1998 by researchers of Lawrence national lab, USA at LOS Alamos Nuclear science centre (LANSCE) [84]. Imaging of 2.54 cm thick Lead (with drill holes) disk sandwiched between 5.08 cm thick uranium slab with a spatial resolution of 1 mm was demonstrated by using a position-sensitive multiwire detector in combination with a tungsten convertor.

Advanced Hybrid Detectors for Neutron Imaging is based on a combination of gas detectors with associated dedicated data acquisition. Though neutron imaging is an old and established technique, with the advent of improved sources such as accelerator-based Spallation Neutrons providing both high intensity and pulsed beams of neutrons newer techniques are being developed to look deeper into materials and processes with high contrast and temporal resolution. Advanced techniques such as energy-resolved neutron imaging, Bragg-edge imaging, resonance imaging have the potential in providing physical and chemical properties in a bulk in addition to its macroscopic 3D volumetric distribution. These are called counting-type imaging detectors. Initial development work [85] on such detector has been reported using Boron-10 (Purity ≥ 99%) coated gas electron multiplication foils stacked in a chamber and coupled to specific ASICs and FPGA . The prototype detector chamber has the following constructional details. Cathode plate for applying HV is made of aluminium, two numbers of B-10 coated GEM foils for neutron interaction, two normal GEM foils for gas gain towards detected signal and the read out boards (ASICs). The initial development though targeted for particle detection has been modified for neutron detection and imaging application. When only the boron coated aluminium is used and no B-10 coated GEM foil, the detector has shown potential application in neutron beam monitor. Using the complete detector i.e. incorporating B-10 coated GEM foils, experiment on energy selective neutron radiography using cold neutron beam from JPARC spallation source has been reported providing spatial resolution ~ 0.8 mm, temporal resolution ~ 10 ns and active imaging area of 10 cm × 10 cm. The experiments have revealed two-dimensional images of iron plates, which have gone through different bending conditions. Recent advances in this domain have resulted in development of various detectors such as μPIC, μNID, nGEM and the LiTA12.

μPIC (micro-pixel chamber) [86] is a micropattern gaseous detector having 400 μm pitch incorporating orthogonal anode and cathode strips for two-dimensional read-out. The chamber has Ar-C_2H_6-^{3}He (63:7:30) gas mixture at 2 atm. Demonstration experiments carried out using μPIC detector at Materials and Life Sciences experimental facility (JPARC) demonstrated its detection efficiency ~ 18% for thermal neutrons, spatial and temporal resolution of 100–120 μm and ~ 0.6 microsec respectively. This detector is developed for time-resolved neutron imaging applications.

μNID [87] has been developed using μPIC micropattern read-out plane coupled to a time projection chamber having an active volume of 100 × 100 × 25 mm^3. The detection is enabled by the gas mixture CF_4–iC_4H_{10}–^{3}He in the ratio of 45:5:50 kept at 2 atm pressure. Complex readout mechanism and analysis involving the μPIC in combination with the arrival time of the neutron along with the deposited energy (above some pre-decided threshold) provides spatial and temporal resolution ~ 100 μm and ~ 250 ns in the μNID. Further developments are being perused towards increasing both the resolutions.

The nGEM detector is a combination of a drift cathode in the time projection chamber and B-10 coated GEM (gas electron multiplier). The B-10 coating is ~ 1 μm. The detector is filled with a gas mixture of Ar-CO_2 (70:30) at 1 atm for its ionization by the charge particles emitted by thermal neutrons interacting with the boron. A pair of normal GEMs amplify this ionization and the signal is then read by FPGA-based data acquisition. The best part of the gas-based counter-type detectors is their very low sensitivity towards gamma rays.

The LiTA12 or ^{6}Li Time Analyzer, Model 2012 is made up of Ce activated Li-glass scintillator pixel (pixel size ~ 2.1 × 2.1 × 1 mm^3) detector coupled pixel-to-pixel with a multi-anode PMT. The scintillations produced by the charge particles generated in neutron interaction with Li are detected by the MA-PMT, converted to electrical signals and digitized by dedicated FPGA modules. Though the detection efficiency reported for this detector is 23%, the spatial resolution is poor (~3 mm) due to the limitation set by individual pixel size. A single scintillator plate when used in place of the Li-glass scintillator pixel assembly, provided improved spatial resolution of ~ 0.7 mm.

Summary

This chapter deals with the basics of various mechanisms of neutron optics employed towards spatial beam shaping, spectral shaping and intensity increase. These developments were driven by the need to carry out imaging for various applications. Once the beam is ready for imaging, one needs imaging detectors. Various detectors developed and are used till date are discussed with the applications intended for their use. With the development of high-intensity reactor or spallation sources, continuous as well as pulsed experiments with extra feature of wavelength dispersive imaging has been employed to dig deeper inside materials and processes related to them. Developments of advanced detectors and their use in these specialized experiments have also been discussed.

References

1. Klein AG, Werner SA (1998) Neutron optics. Rep Prog Phys 46(3):259–339
2. Rostaa L, Füzia J, Hományi L (2004) Neutron physical properties of a multi-blade neutron velocity selector. Physica B 350:e711–e716
3. Longpol I (1974) A long wavelength neutron polarization analysis instrument. In: Camphell SJ, Ahmed N, Hicks TJ, Ebdon FR, Wheeler DA (eds) J Phys E: Sci Instrum 7:195
4. Lushchikov WI et al (1970) J Nucl Phys 10:669
5. Williams WG (1988) Polarized neutrons.Clarendon Press, Oxford
6. Bouchiat M, Carver TR, Varnum CM (1960) Nuclear polarization in He^3 gas induced by optical pumping and dipolar exchange. Phys Rev Lett 5:373
7. Colegrove FD, Schearer LD, Walters GK (1963) Polarization of He3 gas by optical pumping. Phys Rev 132:2561
8. Okudaira T, Oku T, Ino T et al (2020) Development and application of a ^{3}He neutron spin filter at J-PARC. Nucl Inst Methods Phys Res A 977:164301
9. Ott F (2008) Focusing optics for neutrons. In: Erko A, Idir M, Krist T, Michette AG (eds) Modern developments in x-ray and neutron optics. Springer Series in optical science, vol 137. Springer, Berlin. https://doi.org/10.1007/978-3-540-74561-7_7
10. Kumakhov MA, Sharov VA (1992) A neutron lens. Nature 357:390
11. Rai DK, Abir M, Wu H, Khaykovich B, Moncton DE (2018) Focusing mirrors for enhanced neutron radiography with thermalneutrons and application for irradiated nuclear fuel. Nucl Inst Methods Phys Res A 879:141–146
12. Mezei F (1976) Novel polarized neutron devices: supermirror and spin component amplifier. Commun Phys (Lond) 1(3):81–85
13. Schanzer C, Scneider M, Boni P (2016) Neutron optics, towards application s for hot neutrons. J Phys: Conf Ser 746:012024. Accessed on 01 Sept 2021
14. Hosobata T, Yamada NL, Hino M, Yamagata Y, Kawai T, Yoshinaga H, Hori K, Takeda M, Takeda S, Morita S (2017) Development of precision elliptic neutron-focusing supermirror. Opt Express 25:20012–20024. https://doi.org/10.1364/OE.25.020012. Accessed on 01 Sept 2021
15. Lynn JW, Kjems JK, Passell L, Saxena AM, Schoenborn BP (1976) Iron–germanium multilayer neutron polarizing monochromators. J Appl Crystallogr 9:454–459
16. Hoghoj P, Anderson R, Siebrecht R, Graf W, Ben-Saidane B (1999) Neutron polarizing Fe/Si mirrors at ILL. Physica B 267–268:355
17. Schebetov F, Pleshanov NK, Pusenkov VM, Peskov BG, Shmelev GE, Kraan WH, Por PT, Rekveldt MTH, Mikhailova VE (1994) Construction and testing of a multichannel polariser for thermal neutrons. Nucl Instrum Methods B 94:575
18. Clemens D, Boni P, Friedli HP, Gottel R, Fermon C, Grimmer H, van Swygenhoven H, Archer J, Klose F, Krist Th, Mezei F, Thomas P (1995) Polarizing $Ti_{1-u}X_u/Fe_xCo_yV_z$ supermirrors. Physica B 942: 213–214
19. Boni P (1997) Supermirror-based beam devices. Physica B 234–236:1038
20. Eskildsen MR, Gammel PL, Isaacs ED, Detlefs C, Mortensen K, Bishop DJ (1998) Compound refractive optics for the imaging and focusing of low-energy neutrons. Nature 391:563
21. Adachia T, Ikedaa K, Okua T, Guoa J, Lina W, Ohmoria H, Morishimaa T, Shimizua HM, Sakaia K, Suzukic J, Littrelld KC, Loong C-K (2004) Possible application of compound Fresnel lens for neutron beam focusing. Physica B 350:e775–e778
22. Littrell KC, te Velthuis SGE, Felcher GP (2007) Magnetic compound refractive lens for focusing and polarizing cold neutron beams. Rev Sci Instrum 78:035101. https://doi.org/10.1063/1.2709844
23. Cremer JT, Filter H, Klepp J, et al. (2020) Focusing and imaging of cold neutrons with a permanent magnetic lens. Rev Sci Instrum 91:013704. https://doi.org/10.1063/1.5116759
24. https://www.ncnr.nist.gov/instruments/ng7sans/lens.html. Accessed on 27 Aug 2021
25. Shimizu HM et al (1999) Measurement of cold neutron-beam focusing effect of a permanent sextupole magnet. Nuclear Inst Methods Phys Res A 430(2–3):423–434

26. Iwashita Y, Tajima Y, Ichikawaa M, Nakamura S, Ino T, Muto S, Shimizu HM (2008) Variable permanent magnet sextupole lens for focusing of pulsed cold neutrons. Nucl Inst Methods Phys Res A 586(1):73–76
27. Yamada M et al (2009) Development of modulating permanent magnet sextupole lens for focusing of pulsed cold neutrons. Nucl Inst Methods Phys Res A 404(17):2646–2651
28. Iwashita Y et al (2010) Practical applications of permanent magnet multipoles. IEEE Trans Appl Superconduct 20(3):842–845
29. Yamada M et al (2015) Pulsed neutron-beam focusing by modulating a permanent-magnet sextupole lens. Progr Theor Exp Phys 2015(4):043G01
30. http://cis01.central.ucv.ro/pauc/vol/2019_29/5_45_49_2019.pdf. Accessed on 25 Aug 2021
31. Cantargi F, Granada JR, Mayer RE (2015) Thermal neutron scattering kernels for sapphire and silicon single crystals. Ann Nucl Energy 80:43–46
32. Seco J, Clasie B, Partridge M (2014) Review of the characteristics of radiation detectors for dosimetry and imaging. Phys Med Biol 59:R303
33. Lehmann EH et al (2004) Neutron imaging—detector options and practical results. Nucl Instrum Methods Phys Res A 531:228–237
34. https://radiopaedia.org/articles/detective-quantum-efficiency-1. Accessed on 31 May 2021
35. https://eljentechnology.com/products/neutron-detectors/ej-426. Accessed 14 May 2021
36. https://webstore.iec.ch/publication/21937. Accessed 30 May 2021
37. Masalovich S (2019) Analysis of the detective quantum efficiency of a neutron image plate detector. Nucl Instrum Methods Phys Res Sect A: Accelerat Spectrom Detect Associat Equip 930:151–155. ISSN 0168-9002. https://doi.org/10.1016/j.nima.2019.03.094
38. Lewandowski R, Cao L, Turkoglu D (2012) Noise evaluation of a digital neutron imaging device. Nucl Instrume Methods Phys Res Sect A Acceler Spectrom Detect Associat Equip 674:46–50. ISSN 0168-9002. https://doi.org/10.1016/j.nima.2012.01.025
39. Shaikh AM (2008) Pramana J Phys 71(4)–663–672
40. Nimura N (1994) An Imaging plate neutron detector. NIMA 349:521–525
41. https://www.selectscience.net/products/fla-9000-starion/?prodID=84313#tab-2. Accessed date 11 May 2021
42. Massalovitch S, Ioffe A, Kuessel E, Schlapp M, Brueckel T (2002) Appl Phys A 74:118
43. Schlapp M, Conrad H, von Seggern H (2004) Pixelated neutron image plates. J Phys D: Appl Phys 37:2607
44. Mikerov V, Bogolubov E, Samosyuk V, Verushkin S (2006) Fast neutron imaging with CCD detectors and imaging plates. In: International workshop on fast neutron detectors, University of Cape Town, South Africa, April 3–6, 2006
45. Wu C et al (2013) A study of ZnS(Ag)/(LiF)-Li-6 with different mass ratios. Radiat Meas 58:128–132
46. de Beer F et al (2020) Overview of the conceptual design of the upgraded neutron radiography facility (INDLOVU) at the SAFARI-1. In: Research reactor in South Africa, materials research proceedings, vol 15, pp 11–16. https://doi.org/10.21741/9781644900574-2
47. Osovizky A, Pritchard K, Ziegler J, Binkley E, Yehuda-Zada Y, Tsai P, Thompson A, Cooksey C, Siebein K, Hadad N, Jackson M, Hurlbut C, Ibberson R, Baltic GM, Majkrzak CF, Maliszewskyj NC. ^{6}LiF:ZnS(Ag) mixture optimization for a highly efficient ultrathin cold neutron detector. https://doi.org/10.1109/TNS.2018.2809567
48. Nagarkar VV, Tipnis SV, Gaysinskiy V, Klugerman Y, Squillante AR, Entine G (2001) Structured LiI scintillator for thermal neutron imaging. IEEE Trans Nucl Sci 48(6):2330–2334. https://doi.org/10.1109/23.983262
49. Sen I, Penumadu D, Williamson M, Miller LF, Green AD, Mabe AN (2011) Thermal neutron scintillator detectors based on poly (2-Vinylnaphthalene) composite films. IEEE Trans Nucl Sci 58(3):1386–1393. https://doi.org/10.1109/TNS.2011.2141149
50. https://scintacor.com/products/6-lithium-glass/. Accessed date: 20 May 2021
51. Moore ME, Trtik P, Lousteau J, Pugliese D, Brambilla G, Hayward JP (2019) Neutron imaging with Li-glass based multicore SCIntillating FIber (SCIFI). J Lightwave Technol 37(22):5699–5706

52. Trtik P, Lehmann EH (2015) Isotopically-enriched gadolinium-157 oxysulfide scintillator screens for the high-resolution neutron imaging. NIMA 788(11):67–70
53. https://www.rctritec.com/en/scintillators.html
54. Chuirazzi W, Craft A, Schillinger B, Cool S, Tengattini A (2020) Boron-based neutron scintillator screens for neutron imaging. J Imaging 6(11):124. https://doi.org/10.3390/jimaging6110124
55. Craft A, Grünzweig C, Morgano M, Chuirazzi W, Lehmann E (2020) Gamma discriminating scintillation screens for digital transfer method neutron imaging. Mater Res Proc 15:74–79. https://doi.org/10.21741/9781644900574-12
56. Feller WB, Gregory Downing R, White PL (2000) Neutron field imaging with microchannel plates. In: Hard x-ray, gamma-ray, and neutron detector physics II, vol 4141. International Society for Optics and Photonics
57. Tremsin AS, Bruce Feller W, Gregory Downing R (2005) Efficiency optimization of microchannel plate (MCP) neutron imaging detectors. I. Square channels with 10B doping. Nucl Instrum Methods Phys Res Sect A: Accelerat Spectrom Detect Associat Equip 539(1–2):278–311. ISSN 0168-9002. https://doi.org/10.1016/j.nima.2004.09.028
58. Tremsin AS, McPhate JB, Vallerga JV, Siegmund OHW, Hull JS, Feller WB, Lehmann E (2009) High-resolution neutron radiography with microchannel plates: proof-of-principle experiments at PSI. Nucl Instrum Methods Phys Res Sect A: Accelerat Spectrom Detect Associat Equip 605(1–2):103–106. ISSN 0168-9002. https://doi.org/10.1016/j.nima.2009.01.137
59. Medipix Collaboration. http://medipix.cern.ch/MEDIPIX
60. Jakubek J, Holy T, Lehmann E, Pospisil S, Uher J, Vacik J, Vavrik D (2006) Neutron imaging with Medipix-2 chip and a coated sensor. Nucl Instrum Methods Phys Res, Sect A 560(1):143–147
61. Wang Y, Han S, Hao L, He L, Wei G, Wu M, Wang H, Liu Y, Chen D (2013) New type of neutron image scintillator based on $H_3{}^{10}BO_3$/ZnS(Ag). Phys Procedia 43:216–222
62. Shestakova I, Tipnis SV, Gaysinskiy V, Antal JJ, Bobek L, Nagarkar VV (2005) A new sensor for thermal neutron imaging. IEEE Trans Nucl Sci 52(4):1109–1113. https://doi.org/10.1109/TNS.2005.852671
63. https://www.saint-gobain.com/en. Accessed date 16 May 2021
64. Hall J (2001) Science & Technology Report
65. Johnson MS, Anderson SG, Bleuel DL, Fitsos PJ, Gibson D, Hall JM, Marsh R, Rusnak B, Sain J (2017) Development of a high-brightness, Quasi-monoenergetic neutron source for neutron imaging. Phys Procedia 90:47–54
66. Adams R, Zboray R, Prasser H-M (2016) A novel fast-neutron tomography system based on a plastic scintillator array and a compact D-D neutron generator. Appl Radiat Isot 107:1–7
67. Bishnoi S, Sarkar PS, Thomas RG et al (2019) Preliminary experimentation of fast neutron radiography with D-T neutron generator at BARC. J Nondestruct Eval 38:13. https://doi.org/10.1007/s10921-018-0550-9
68. Lehman E et al (2021) Improvement in the spatial resolution for imaging with fast neutron. NIMA 988:164809
69. Merrill FE, Bower D, Buckles R, Clark DD, Danly CR, Drury OB, Dzenitis JM, Fatherley VE, Fittinghoff DN, Gallegos R, Grim GP, Guler N, Loomis EN, Lutz S, Malone RM, Martinson DD, Mares D, Morley DJ, Morgan GL, Oertel JA, Tregillis IL, Volegov PL, Weiss PB, Wilde CH, Wilson DC (2012) The neutron imaging diagnostic at NIF (invited). Rev Sci Instrum 83:10D317
70. Fittinghoff DN, Bower DE, Drury OB, Dzenitis JM, Hatarik R, Merrill FE, Grim GP, Wilde CH, Wilson DC, Landoas O, Caillaud T, Bourgade J, Buckles RA, Lee J, Weiss PB (2011) Performance improvements to the neutron imaging system at the national ignition facility, LLNL-TR-503351, 6 October 2011
71. Yanagida T, Kawaguchi N, Fujimoto Y, Fukuda K, Yokota Y, Yamazaki Y, Watanabe K, Pejchal J, Uritani A, Iguchi T, Yoshikawa A (2011) Basic study of europium doped LiCaAlF6 scintillator and its capability for thermal neutron imaging application. Opt Mater 33(8):1243–1247. ISSN 0925-3467. https://doi.org/10.1016/j.optmat.2011.02.016

72. Yoshikawa A, Yanagida T, Yokota Y, Kawaguchi N, Ishizu S, Fukuda K, Suyama T, Kim KJ, Pejchal J, Nikl M, Watanabe K, Miyake M, Baba M, Kamada K, Nucl IEEE (2009) Trans Sci 56:3796
73. Yanagida T, Yoshikawa A, Yokota Y, Maeo S, Kawaguchi N, Ishizu S, Fukuda K, Suyama T (2009) Opt Mater 32:311
74. Iwanowska J, Swiderski L, Moszynski M, Yanagida T, Yokota Y, Yoshikawa A, Fukuda K, Kawaguchi N, Ishizu S (2011) Nucl Instr Methods A 652:319
75. Yamazaki A, Watanabe K, Uritani A, Iguchi T, Kawaguchi N, Yanagida T, Fujimoto Y, Yokota Y, Kamada K, Fukuda K, Suyama T, Yoshikawa A (2011) Nucl Instr Methods A 652:435–438
76. Tyagi M, Sarkar PS, Singh AK, Kalyani, Patel T, Bishnoi S, Ray NK, Desai DG, Gadkari SC (2019) Development of neutron detector based on Gd3Ga3Al2O12:Ce single crystals. IEEE Trans Nucl Sci 66(4):724–728
77. Lehmann E, Vontobel P (2004) The use of amorphous silicon flat panels as detector in neutron imaging. Appl Radiat Isot 61(4):567–571
78. Lehmann EH, Vontobel P, Frei G, Brönnimann C (2004) Neutron imaging—detector options and practical results. Nucl Instrum Methods Phys Res, Sect A 531(1–2):228–237
79. Yu B, Harder JA, Mead JA, Radeka V, Schaknowski NA, Smith GC (2003) Neutron detector development at Brookhaven. Nucl Instrum Methods Phys Res Sect A: Accelerat Spectrom Detect Associat Equip 513(1–2):362–366
80. Schaknowski N, Fried J, Smith G, Mahler G, Yu B (2018) Design and construction of a 1m × 1m thermal neutron imager operating in ionization mode with Pad Readout. In: 2018 IEEE nuclear science symposium and medical imaging conference held at Sydney Australia. Brookhaven National Laboratory, Upton, NY, USA, 10–17 November 2018, BNL-211410-2019-PUCP. https://www.osti.gov/servlets/purl/1619254. Accessed date 10 May 2021
81. Tian LC, Chen YB, Tang B, Zhou JR, Qi HR, Liu RG, Zhang J, Yang GA, Xu H, Chen DF, Sun ZJ (2021) Study on the imaging ability of the 2D neutron detector based on MWPC. https://arxiv.org/pdf/1305.5011.pdf . Accessed date 9 May 2021
82. Strobl M, Steitz R, Kreuzer M, Rose M, Herrlich H, Mezei F, Grunze M, Dahint R (2011) BioRef: a versatile time-of-flightreflectometer for soft matter applications at Helmholtz-Zentrum Berlin. Rev Sci Instrum 82:055101. https://doi.org/10.1063/1.3581210
83. Strobl M, Woracek R, Kardjilov N, Hilger A, Wimpory R, Tremsin A, Wilpert T, Schulz C, Manke I, Penumadu D (2012) Time-of-flight neutron imaging for spatially resolved strain investigations. Nucl Inst Methods Phys Res A 680:27–34
84. UCRL-JC-124401, 11 Sept 1996
85. Uno S, Uchida T, Sekimoto M, Murakami T, Miyama K, Shojic M, Nakano E, Koike T (2012) Development of a two-dimensional gaseous detector for energy-selective neutron radiography. Phys Procedia 37(600–605):1875–3892
86. Parker JD, Harada M, Hattori K, Iwaki S, Kabuki S, Kishimoto Y, Kubo H, Kurosawa S, Matsuoka Y, Miuchi K, Mizumoto T, Nishimura H, Oku T, Sawano T, Shinohara T, Suzuki J, Takada A, Tanimori T, Ueno K (2013) Spatial resolution of a μPIC-based neutron imaging detector. Nucl Instrum Methods Phys Res Sect A: Accelerat Spectrom Detect Associat Equip 726:155–161. ISSN 0168-9002. https://doi.org/10.1016/j.nima.2013.06.001
87. Shinohara T, Kai T, Oikawa K, Nakatani T, Segawa M, Hiroi K, Yuhua S, Ooi M, Harada M, Iikura H, Hayashida H, Parker JD, Matsumoto Y, Kamiyama T, Sato H, Kiyanagi Y (2020) The energy-resolved neutron imaging system. RADEN Rev Sci Instrum 91:043302. https://doi.org/10.1063/1.5136034